arXiv:2301.02209v1 [astro-ph.GA] 5 Jan 2023

Spatially Resolved Stellar Populations of $0.3 < z < 6.0$ Galaxies in WHL0137−08 and MACS0647+70 Clusters as Revealed by JWST: How do Galaxies Grow and Quench Over Cosmic Time?

ABDURRO'UF [1,2] DAN COE [2,3,1] INTAE JUNG [2] HENRY C. FERGUSON [2] GABRIEL BRAMMER [4,5]
KARTHEIK G. IYER [6,*] LARRY D. BRADLEY [2] PRATIKA DAYAL [7] ROGIER A. WINDHORST [8] ADI ZITRIN [9]
ASHISH KUMAR MEENA [9] MASAMUNE OGURI [10,11] JOSE M. DIEGO [12] VASILY KOKOREV [7] PAOLA DIMAURO [13]
ANGELA ADAMO [14] CHRISTOPHER J. CONSELICE [15] BRIAN WELCH [16,17,18] EROS VANZELLA [19]
TIGER YU-YANG HSIAO [1] JINMI YOON [2,20] XINFENG XU [1] NAMRATA ROY [1] AND CELIA R. MULCAHEY [1]

[1] *Center for Astrophysical Sciences, Department of Physics and Astronomy, The Johns Hopkins University, 3400 N Charles St. Baltimore, MD 21218, USA*
[2] *Space Telescope Science Institute (STScI), 3700 San Martin Drive, Baltimore, MD 21218, USA*
[3] *Association of Universities for Research in Astronomy (AURA), Inc. for the European Space Agency (ESA)*
[4] *Cosmic Dawn Center (DAWN), Copenhagen, Denmark*
[5] *Niels Bohr Institute, University of Copenhagen, Jagtvej 128, Copenhagen, Denmark*
[6] *Columbia Astrophysics Laboratory, Columbia University, 550 West 120th Street, New York, NY 10027, USA*
[7] *Kapteyn Astronomical Institute, University of Groningen, P.O. Box 800, 9700 AV Groningen, The Netherlands*
[8] *School of Earth and Space Exploration, Arizona State University, Tempe, AZ 85287-1404, USA*
[9] *Physics Department, Ben-Gurion University of the Negev, P.O. Box 653, Be'er-Sheva 84105, Israel*
[10] *Center for Frontier Science, Chiba University, 1-33 Yayoi-cho, Inage-ku, Chiba 263-8522, Japan*
[11] *Department of Physics, Graduate School of Science, Chiba University, 1-33 Yayoi-Cho, Inage-Ku, Chiba 263-8522, Japan*
[12] *Instituto de Física de Cantabria (CSIC-UC). Avda. Los Castros s/n. 39005 Santander, Spain*
[13] *INAF - Osservatorio Astronomico di Roma, via di Frascati 33, 00078 Monte Porzio Catone, Italy*
[14] *Department of Astronomy, Oskar Klein Centre, Stockholm University, AlbaNova University Centre, SE-106 91 Stockholm, Sweden*
[15] *Jodrell Bank Centre for Astrophysics, University of Manchester, Oxford Road, Manchester UK*
[16] *Department of Astronomy, University of Maryland, College Park, MD 20742, USA*
[17] *Observational Cosmology Lab, NASA Goddard Space Flight Center, Greenbelt, MD 20771, USA*
[18] *Center for Research and Exploration in Space Science and Technology, NASA/GSFC, Greenbelt, MD 20771*
[19] *INAF – OAS, Osservatorio di Astrofisica e Scienza dello Spazio di Bologna, via Gobetti 93/3, I-40129 Bologna, Italy*
[20] *Joint Institute for Nuclear Astrophysics - Center for the Evolution of the Elements, USA*

Submitted to ApJ

ABSTRACT

We study the spatially resolved stellar populations of 444 galaxies at $0.3 < z < 6.0$ in two clusters (WHL-0137-08 and MACS0647+70) and a blank field, combining imaging data from *HST* and *JWST* to perform spatially resolved spectral energy distribution (SED) modeling using PIXEDFIT. The high spatial resolution of the imaging data combined with magnification from gravitational lensing in the cluster fields allows us to resolve some galaxies to sub-kpc scales (for 109 of our galaxies). At redshifts around cosmic noon and higher ($2.5 \lesssim z \lesssim 6.0$), we find mass doubling times to be independent of radius, inferred from flat specific star formation rate (sSFR) radial profiles and similarities between the half-mass and half-SFR radii. At lower redshifts ($1.5 \lesssim z \lesssim 2.5$), a significant fraction of our star-forming galaxies show evidence for nuclear starbursts, inferred from centrally elevated sSFR, and a much smaller half-SFR radius compared to the half-mass radius. At later epochs, we find more galaxies suppress star formation in their center but are still actively forming stars in the disk. Overall, these trends point toward a picture of inside-out galaxy growth consistent with theoretical models and simulations. We also observe a tight relationship between the central mass surface density and global

Corresponding author: Abdurro'uf
fabdurr1@jhu.edu

stellar mass with ~ 0.38 dex scatter. Our analysis demonstrates the potential of spatially resolved SED analysis with JWST data. Future analysis with larger samples will be able to further explore the assembly of galaxy mass and the growth of their structures.

1. INTRODUCTION

Over the last few decades, multiwavelength studies of galaxies throughout cosmic history reveal that the global star formation rate density (SFRD) in the universe was increasing with cosmic time from the reionization epoch and reached a peak at $z \sim 2$ (~ 3.5 Gyr after the Big Bang; cosmic noon) after which it declined exponentially toward the present day (Madau & Dickinson 2014). In this picture, it is estimated that $\sim 25\%$ of the present-day stellar mass density (SMD) was formed before the peak of the cosmic SFRD, around half of the SMD was formed during $0.7 < z < 2.0$, and another $\sim 25\%$ was formed since $z = 0.7$ (i.e., around the last half of the universe's age; Madau & Dickinson 2014). Although the cosmic SFRD at early cosmic time is still debated due to the dust obscuration effects (see e.g., Fudamoto et al. 2021; Casey et al. 2018), an emerging picture is that cosmic SMD increases with cosmic time since the epoch of reionization, which is believed to take place before $z \sim 6$ (e.g., Treu et al. 2013; McGreer et al. 2015; Dayal & Ferrara 2018).

Observations also revealed that most of the star formation occurs in galaxies that lie in the so-called star-forming main sequence (SFMS), which is a tight nearly linear correlation between the integrated (i.e., global) star formation rate (SFR) and stellar mass (M_*; Brinchmann et al. 2004; Daddi et al. 2007; Elbaz et al. 2007; Noeske et al. 2007; Whitaker et al. 2012, 2014; Speagle et al. 2014; Salmon et al. 2015; Tomczak et al. 2016; Santini et al. 2017; Iyer et al. 2018; Leja et al. 2022). This relation has been shown to hold at any epoch with a nearly constant scatter (~ 0.3 dex; Whitaker et al. 2012; Speagle et al. 2014), suggesting that galaxies grow in mass over cosmic time in a state of self-regulated semi-equilibrium (e.g., Bouché et al. 2010; Daddi et al. 2010; Genzel et al. 2010; Tacchella et al. 2016b, 2020). Understanding this process in detail as well as the mechanisms that shut down star formation in galaxies and move them out of the SFMS onto the "quenched" population requires knowledge of not only integrated galaxy

* Hubble Fellow

properties but also spatially resolved structures within galaxies.

The study of spatially resolved properties of galaxies with integral field spectroscopy (IFS) and high spatial resolution imaging have been providing important insights toward a better understanding of galaxy evolution. Among the important findings is the realization that some of the well-known scaling relations observed on global scales are originated from similar relations on kpc scales within galaxies (see a review by Sánchez 2020). This includes the spatially resolved star-forming main sequence relation, a relationship between SFR surface density ($\Sigma_{\rm SFR}$) and M_* surface density (Σ_*), which is thought to be more fundamental than the global SFMS (e.g., Sánchez et al. 2013; Wuyts et al. 2013; Cano-Díaz et al. 2016; Abdurro'uf & Akiyama 2017; Hsieh et al. 2017; Abdurro'uf & Akiyama 2018; Lin et al. 2019; Morselli et al. 2020; Abdurro'uf et al. 2022b). This emphasizes the necessity of studying the spatially resolved properties of galaxies.

Spatially resolved studies of high redshift galaxies ($z \sim 1 - 4$) have hinted on how galaxies assembled their structures. The emerging picture from these studies is that galaxies grow their mass in an inside-to-outside manner (i.e., *inside-out growth* scenario; e.g., van Dokkum et al. 2013; Nelson et al. 2012; Morishita et al. 2015; Nelson et al. 2016) and cease their star formation activities in a similar manner (i.e., *inside-out quenching* scenario; e.g., Tacchella et al. 2015; Jung et al. 2017; Abdurro'uf & Akiyama 2018; Tacchella et al. 2018). Nelson et al. (2016) analyzed the spatially resolved distributions (on kpc scales) of Hα emission and M_* of $0.7 < z < 1.5$ galaxies using the Hubble Space Telescope (*HST*)/WFC3 grism data from the 3D-HST survey (Skelton et al. 2014). They found that the spatial distribution of H_α emission in the galaxies is more extended than the stellar mass, suggesting that the past star formation in the galaxies have accumulated stellar mass in the center and now the star formation progresses outward to assemble the disk. Tacchella et al. (2015) analyzed the spatial distributions of SFR and M_* of ~ 30 star-forming galaxies at $z \sim 2$ using IFS data from the SINS/zC-SINF survey (Förster Schreiber et al. 2018). They observed that massive galaxies ($M_* \gtrsim 10^{11} M_\odot$)

in their sample have a centrally-suppressed specific SFR (sSFR) radial profile and a massive central spheroid that is as dense as the centers of local early-type galaxies. In contrast to this, less massive galaxies in their sample have broadly flat sSFR radial profiles. This trend indicates that massive galaxies at this epoch might have started a quenching process in their central regions and assembled a mature bulge.

The buildup of the central stellar mass density is likely correlated with the quenching process in galaxies. The central stellar mass density within a 1 kpc radius ($\Sigma_{*,1\rm kpc}$) has been shown to be a good predictor for quiescence, where galaxies with high $\Sigma_{*,1\rm kpc}$ are tend to be red and quiescent, whereas galaxies with low $\Sigma_{*,1\rm kpc}$ are tend to be blue and star-forming (e.g., Fang et al. 2013; Tacchella et al. 2015, 2016a; Barro et al. 2017; Jung et al. 2017; Whitaker et al. 2017). It has also been shown that $\Sigma_{*,1\rm kpc}$ is tightly correlated with the global M_*, suggesting that M_* of galaxies grow hand-in-hand with the central mass density. In this $\Sigma_{*,1\rm kpc}$–M_* relation, quiescent galaxies reside in a sequence at the tip of the overall relation and have a shallower slope than the relation with star-forming galaxies only, indicating a formation of a matured bulge in the quiescent galaxies (Fang et al. 2013; Tacchella et al. 2015; Barro et al. 2017).

Galaxies also grow their sizes hand-in-hand with the global M_*, as indicated by the size–mass relation (e.g., Shen et al. 2003; van der Wel et al. 2014; Suess et al. 2019). Previous studies have shown that star-forming and quiescent galaxies follow very different size–mass relations where quiescent galaxies tend to be more compact (i.e., having smaller size) in all M_* and exhibit steeper relation than the star-forming galaxies (van der Wel et al. 2014; Yang et al. 2021). A possible explanation for this trend is that star-forming galaxies build their mass at all radii by mostly in-situ star formation, whereas quiescent galaxies grow inside-out through mergers (e.g., van Dokkum et al. 2015).

Previous studies, some of which are mentioned above, have used HST for resolving galaxies out to $z \sim 3$, roughly a limit where galaxies can be resolved well by the telescope, given its spatial resolution and depth. Furthermore, the wavelength coverage of HST only covers the rest-frame ultraviolet (UV) and a small portion of the optical at $z \sim 3$, making it difficult to robustly derive the stellar mass as well as the other stellar population properties, which typically requires a rest-frame near-infrared (NIR). Forcing to include NIR imaging from the ground-based telescopes would need to sacrifice the spatial resolution of HST (e.g., Jung et al. 2017). With the advent of the James Webb Space Telescope ($JWST$)

NIRCam observations (Rigby et al. 2022), with its high spatial resolution, depth, and its coverage in NIR, now we can push the analysis of spatially resolved SED of galaxies to higher redshifts. Some very recent studies have used $JWST$/NIRCam imaging to study the internal structures and morphology of galaxies at $z > 3$ (e.g., Ferreira et al. 2022; Chen et al. 2022; Kartaltepe et al. 2022; Giménez-Arteaga et al. 2022), and even resolving a lensed galaxy at $z \sim 11$ (Hsiao et al. 2022).

In this paper, we use imaging data from HST/ACS and $JWST$/NIRCam to analyze the spatially resolved SEDs of $0.3 < z < 6.0$ galaxies in the sightlines of WHLJ013719.8–082841 (hereafter WHL0137−08; RA = 01:37:25.0, DEC = −08:27:23, J2000; $z = 0.566$; Wen et al. 2012; Wen & Han 2015) and MACSJ0647.7+7015 (hereafter MACS0647+70; RA = 06:47:50.03, DEC = +70:14:49.7, J2000; $z = 0.591$; Ebeling et al. 2007) clusters and examine the spatial distributions of their stellar populations. Our main goal is to get hints on the assembly of galaxy structures over cosmic time, especially how galaxies build their stellar masses and quench their star formation activities. The high spatial resolution of $JWST$/NIRCam combined with magnification from gravitational lensing in the cluster fields, allow us to resolve high-redshift galaxies down to sub-kpc scales. Our method using PIXEDFIT (Abdurro'uf et al. 2022c) can simultaneously process imaging data, perform pixel binning to optimize the signal-to-noise (S/N) ratio of the spatially resolved SEDs, and perform SED fitting. The wavelength coverage of HST/ACS and $JWST$/NIRCam allow us to get full coverage of the rest-frame UV to NIR for the majority of our sample, which can give a strong constraint on model SEDs and break the age–dust–metallicity degeneracy (see Appendix B). While IFS observation at $z \gtrsim 2$ is lacking, our analysis in this paper provides a good alternative for the analysis of spatially resolved SED of high redshift galaxies using $JWST$/NIRCam imaging data. Our analysis in this paper is one of the first robust spatially resolved SED analyses of hundreds of galaxies using $JWST$ data. Abdurro'uf et al. (2021) have demonstrated the capabilities of spatially resolved SED fitting using PIXEDFIT on local galaxies. In particular, it gives robust SFR on kpc scales when rest-frame UV to NIR photometry is available, which is consistent with the SFR derived from Hα emission maps (dust-corrected based on the Balmer decrement) from the MaNGA IFS survey (Bundy et al. 2015).

The paper is organized as follows. In Section 2, we present the data and sample galaxies. We describe the spatially resolved SED fitting methodology in Section 3 and present our results in Section 4, which include the

radial profiles of some key stellar population properties, comparison between the compactness of the spatial distributions of SFR and M_*, and $\Sigma_{*,1\text{kpc}}-M_*$ relation. In Section 5, we further discuss our results, focusing on the evolutionary trends with redshift and what the implications to the study of galaxy evolution.

Throughout this paper, we assume the Chabrier (2003) initial mass function (IMF) with a mass range of $0.1 - 100 M_\odot$ and cosmological parameters of $\Omega_m = 0.3$, $\Omega_\Lambda = 0.7$, and $H_0 = 70$ km s^{-1} Mpc^{-1}.

2. DATA AND SAMPLE

2.1. *Observational Data*

2.1.1. *JWST Observations*

We obtain *JWST*/NIRCam imaging data of WHL0137−08 cluster from Cycle 1 General Observers (GO) 2282 program (PI Coe) and MACS0647+70 cluster from GO 1433 program (PI Coe). The WHL0137−08 cluster was observed in July 2022, while the MACS0647+70 cluster was observed in 23 September 2022. The GO 2282 program aims at further investigating Earendel (Welch et al. 2022a,b) and the Sunrise Arc (Vanzella et al. 2022). The *JWST*/NIRCam data from this program consist of eight filters (F090W, F115W, F150W, F200W, F277W, F365W, F410M, and F444W) spanning a wavelength range of $0.8 - 5.0$ μm. The GO 1433 program is intended to observe the triply-lensed galaxy MACS0647–JD at $z \sim 11$ (Coe et al. 2013; Hsiao et al. 2022). This program obtained *JWST*/NIRCam imaging in six filters (F115W, F150W, F200W, F277W, F365W, and F444W) spanning $1 - 5$ μm. The exposure time of each filter in the two programs is 2104 seconds. It achieves 5σ limiting AB magnitude of 28.0 to 29.0 in a $r = 0\rlap{.}''2$ diameter circular aperture.

For each filter, we obtained four dithers using IN-TRAMODULEBOX primary dithers to cover the $4-5''$ gap between the sort wavelength (SW; $\lambda < 2.4\mu$m) detectors, improve the spatial resolution of final drizzled images, and minimize the impact of image artifacts and bad pixels. We obtained NIRCam imaging over two $2\rlap{.}'26 \times 2\rlap{.}'26$ fields separated by $40\rlap{.}'5$, covering a total area of 10.2 arcmin^2. In the observation of WHL0137−08 cluster, the NIRCam module B was centered at the cluster while the module A covered a nearby field centered $\sim 2\rlap{.}'9$ from the cluster center (hereafter called "blank field"). On the other hand, the MACS0647+70 cluster was centered at the module A and the module B observes a blank field nearby to it.

2.1.2. *HST Data*

We obtain *HST* imaging data of the WHL0137−08 cluster from the Reionization Lensing Cluster Survey (RELICS) *HST* Treasury program (GO 14096; Coe et al. 2019). THe RELICS program obtained the first *HST* imaging of the WHL0137−08 cluster in 2016 with three orbits of ACS (F435W, F606W, and F814W) and two orbits of WFC3/IR (F105W, F125W, F140W, and F160W) data spanning $0.4 - 1.7$ μm. Two follow-up *HST* imaging programs (GO 15842 and GO 16668; PI: Coe) have thus far obtained an additional 5 orbits of *HST* ACS imaging in F814W, 2 orbits in F475W, and 4 orbits with WFC3/IR in F110W. The *HST* imaging data only cover the WHL0137−08 cluster field. Therefore, we do not have HST imaging data for the blank field.

The *HST* imaging data of the MACS0647+70 cluster are taken from multiple programs. Overall, MACS0647+70 has been observed in total of 39 orbits of *HST* imaging in 17 filters. The cluster was first observed by programs GO 9722 (PI Ebeling) and GO 10493, 10793 (PI Gal-Yam) in the ACS F555W and F814W filters. Then additional imaging in 15 filters (WFC3/UVIS, ACS, and WFC3/IR, spanning $0.2 - 1.7$ μm) was obtained by the Cluster Lensing and Supernova Survey with Hubble (CLASH; Postman et al. 2012; GO 12101, PI Postman). Finally, additional imaging in WFC3/IR F140W was obtained as part of a grism spectroscopy program (GO 13317, PI Coe).

It is important to note that the nearby blank fields to the WHL0137−08 and MACS0647+70 clusters that are observed with NIRCam are not covered in the *HST* observations described above. In this work, we analyze galaxies in three fields: WHL0137−08 cluster field, MACS0647+70 cluster field, and the NIRCam blank field nearby to the WHL0137−08 (hereafter simply called blank field). We do not analyze galaxies in the NIRCam blank field of MACS0647+70 because it is observed in less number of NIRCam filters than the blank field of WHL0137−08 and it does not have F090W observation, which prevents us from selecting galaxies at $z < 2$ in this field as their photometry do not cover the rest-frame 4000 Å break. For the WHL0137−08 and the blank field, we use 4 *HST*/ACS filters (F435W, F475W, F606W, and F814W) and 8 *JWST*/NIRCam filters, whereas for the MACS0647+70, we use 7 *HST*/ACS filters (F435W, F475W, F555W, F606W, F625W, F775W, and F814W) and six *JWST*/NIRCam filters. We do not use *HST*/WFC3 IR filters to get high spatial resolution possible while still get sufficiently wide wavelength coverage with the *HST*/ACS and *JWST*/NIRCam. Please refer to Table 1 for information on limiting magnitudes

Table 1. *HST* and *JWST* Imaging Data Used in the Spatially Resolved SED Fitting

Telescope	Camera	Filter	Wavelength	Depth[a]		PSF FWHM[b]	
				WHL0137−08	MACS0647+70	WHL0137−08	MACS0647+70
			(μm)	(AB mag)	(AB mag)	(arcsec)	(arcsec)
HST	ACS/WFC	F435W	0.37–0.47	27.7	28.0	0.11	0.11
HST	ACS/WFC	F475W	0.4–0.55	28.5	28.2	0.11	0.11
HST	ACS/WFC	F555W	0.46–0.62	$\cdots$	28.7	$\cdots$	0.11
HST	ACS/WFC	F606W	0.47–0.7	28.3	28.3	0.11	0.11
HST	ACS/WFC	F625W	0.54–0.71	$\cdots$	27.9	$\cdots$	0.11
HST	ACS/WFC	F775W	0.68–0.86	$\cdots$	27.8	$\cdots$	0.08
HST	ACS/WFC	F814W	0.7–0.95	28.7	28.5	0.11	0.11
JWST	NIRCam	F090W	0.8–1.0	28.3	$\cdots$	0.04	$\cdots$
JWST	NIRCam	F115W	1.0–1.3	28.4	28.1	0.04	0.04
JWST	NIRCam	F150W	1.3–1.7	28.5	28.3	0.06	0.06
JWST	NIRCam	F200W	1.7–2.2	28.7	28.4	0.06	0.06
JWST	NIRCam	F277W	2.4–3.1	29.1	28.9	0.11	0.11
JWST	NIRCam	F356W	3.1–4.0	29.3	29.0	0.11	0.11
JWST	NIRCam	F410M	3.8–4.3	28.6	$\cdots$	0.16	$\cdots$
JWST	NIRCam	F444W	3.8–5.0	29.0	28.8	0.16	0.16

NOTE— [a]5σ point source AB magnitude limit measured within a $0\farcs2$ diameter circular aperture. [b]PSF FWHM here are based on empirical measurement as described in Appendix C.

and the point spread function (PSF) sizes of our *HST* and *JWST* data.

2.2. *Sample Galaxies*

We use GRIZLI v4 photometric catalogs (will be described in Section 3.1) to select our sample galaxies in the three fields (WHL0137−08, blank field, and MACS0647+70). The catalogs provide the aperture fluxes and photometric redshifts with which we select our sample. The sample selection is described in the following. First, we select galaxies that have integrated signal-to-noise (S/N) ratio > 5 in all *JWST* filters that are available for the fields. This is to ensure that we will have galaxies with good photometry in at least *JWST* filters. This initial cut selects 1322 (out of 2718), 1278 (out of 3032), and 1331 (out of 2660) galaxies in the WHL0137−08, blank field, and MACS0647+70, respectively. We do not apply the same S/N criteria on *HST* filters because it will exclude many more galaxies as they have lower S/N than *JWST* filters.

We further cut the sample galaxies based on their redshift to get a sufficient coverage of the rest-frame UV–NIR. For galaxies in the WHL0137−08 and MACS0647+70, which are observed by both *JWST* and *HST*, we select galaxies at $0.3 < z < 6.0$, whereas for galaxies in the blank field, which do not have *HST* observations, we select galaxies at $1.3 < z < 6.0$. This

redshift cut ensures that the rest-frame 4000 Åbreak is covered. This cut further reduces the sample to be 1258, 581, and 1257 galaxies in the WHL0137−08, blank field, and MACS0647+70, respectively. After that, we do a visual inspection to exclude galaxies that appear to be very small (i.e., unresolved) and in a merger (i.e., one segmentation region having multiple cores or multiple galaxies in one segmentation region, despite possible interlopers). This further reduce the sample to be 354, 239, 220 galaxies in the WHL0137−08, blank field, and MACS0647+70, respectively.

We perform spatially resolved SED analysis on the galaxies in this initial sample. A detailed description of the methodology will be given in Section 3. Once the analysis is done, we inspect the results of all the galaxies and further exclude galaxies that seem to have bad SED fitting results based on the χ^2 values of the fitting to the integrated SEDs within the central effective radius (see Section 3.5) and the average χ^2 values of the fitting to the first 20 spatial bins (see Section 3.4 for definition of spatial bin). We exclude galaxies that have $\chi^2 > 20$ for the SEDs within the central effective radius and average $\chi^2 > 40$ for the first 20 spatial bins. We note that χ^2 value can be unrealistically high if systematic uncertainties of the photometry are not properly accounted. Beside this, there is still uncertainty around the zero-

point calibration of NIRCam photometry in the current early observations (e.g., Boyer et al. 2022; Finkelstein et al. 2022). Therefore, we visually inspect SED fitting results of each galaxy using similar plots as shown in Figure 4. We find that in most cases, NIRCam fluxes are well fitted by our models, better than HST/ACS fluxes. This might be due the shallower depths (and lower S/N) of HST compared to $JWST$. The χ^2 values above are high enough to get sufficient number of galaxies and low enough to get good quality of SED fitting results. This results in our final sample, consisting of 243, 91, and 110 galaxies in the WHL0137−08, blank field, and MACS0647+70, respectively. Figure 1 shows the distributions of redshifts and M_* of our sample galaxies.

We note that our sample selection may possibly bias toward selecting relatively massive, bright, and resolved galaxies in each redshift. However, due to the lensing magnification in the cluster fields, we expect to detect on average lower mass galaxies with better spatial resolution than in the standard fields. The small number of galaxies and the limited volume sampled might make our sample to be not representative of the general population of galaxies. However, since we do not make inferences on the average trends or number densities as function of global properties (e.g., M_*), but instead we show trends in individual galaxies, our results still provide useful insights on the evolution of galaxy structures. We also ignore the possible contamination by the Active Galactic Nucleus (AGN) host galaxies in our current study because of the lack of diagnostics for identifying them using our current data.

3. METHODOLOGY

3.1. Data Reduction and Photometric Catalog

We use the GRIZLI pipeline (Brammer et al. 2022) to process the HST FLT and the $JWST$ pipeline-calibrated level-2 imaging data. The $JWST$ data were processed using the calibration pipeline v1.5.3 with CRDS context jwst_0942.pmap, which includes photometric calibrations based on in-flight data. The $JWST$ level-2 imaging data were then scaled with detector-dependent factors[1] based on a NIRCam flux calibration using the standard star J1743045. Our photometric zeropoints described here are similar to those obtained by the $JWST$ Resolved Stellar Populations ERS program (Boyer et al. 2022; Nardiello et al. 2022) who analyzed the M92 globular cluster. We also check the consistency of our calibration with the more recent one based on CAL program
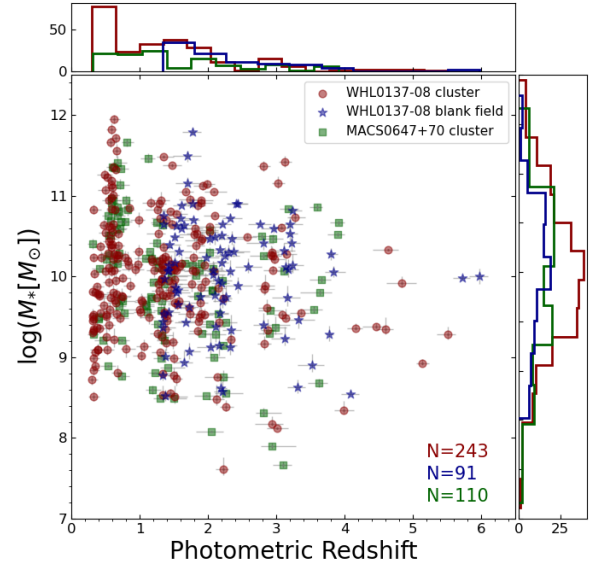
Figure 1. Distributions of M_* and redshifts of the sample galaxies analyzed in this work that consist of galaxies in WHL0137−08 cluster field, a blank field (i.e., a nearby field of the WHL0137−08 that is observed with NIRCam), and MACS0647+70 cluster field. The M_* here are derived by summing up M_* of pixels (in the galaxy's region) obtained from our spatially resolved SED analysis.

data jwst_0989.pmap and find out that they are consistent within 3% in all filters analyzed here.

In processing the $JWST$ data, the GRIZLI pipeline applies a correction to reduce the effect of $1/f$ noise and masks "snowballs"[2] effect caused by the large cosmic ray impacts to the NIRCam detectors. Beside this, the GRIZLI pipeline also corrects for the "wisps"[3], which is a faint, diffuse stray light features that appear at the same detector locations in NIRCam images and most prominent in the A3, B3, and B4 detectors in the F150W and F200W images.

The GRIZLI pipeline aligns the HST and $JWST$ imaging data to a common world coordinate system which is registered based on the GAIA DR3 catalogs (Gaia Collaboration et al. 2021). The images are then drizzled to a common pixel grid using the ASTRODRIZZLE (Koekemoer et al. 2003; Hoffmann et al. 2021). The 17 HST filters and 4 $JWST$ NIRCam long-wavelength (LW) filters (F277W, F356W, F410M, and F444W) are drizzled

to a spatial sampling of $0\!\!''04$ per pixel while the *JWST* short-wavelength (SW) filters (F090W, F115W, F150W, and F200W) are drizzled to a spatial sampling of $0\!\!''02$ per pixel.

Source detection is then performed on a weighted sum of the drizzled NIRCam images in all filters using SEP (Barbary 2016; Bertin & Arnouts 1996). Fluxes are then calculated for each source in three circular apertures, $0\!\!''36$, $0\!\!''5$, and $0\!\!''7$. Then photometric redshift measurement is performed using the $0\!\!''5$ aperture SEDs employing EAZYPY (Brammer et al. 2008). This code fits observed photometry using a set of templates added in a non-negative linear combination. The processed imaging data along with the photometric catalog are publicly available[4]. These data product have also been used in some recent studies (Welch et al. 2022b; Bradley et al. 2022b; Hsiao et al. 2022; Vanzella et al. 2022; Meena et al. 2022).

3.2. *Analysis of Post-processed Imaging Data*

In this work, we combine the post-processed *HST* and *JWST* imaging data (in up to 13 filters) into a common spatial resolution (i.e., PSF size) and sampling (i.e., pixel size) for extracting the spatially resolved SEDs of our sample galaxies. These spatially resolved SEDs are then fitted with models to infer the underlying properties of the stellar populations. We use PIXEDFIT[5] (Abdurro'uf et al. 2021, 2022c) throughout this analysis. Basically, this process includes three main tasks: image processing, pixel binning, and SED fitting. We will briefly describe these steps in the following.

The image processing is carried out automatically using PIXEDFIT. For each galaxy, we first crop stamp images with a size of $6\!\!''04 \times 6\!\!''04$ (corresponding to $302{\times}302$ pixels in NIRCam SW and $151{\times}151$ pixels in NIRCam LW and *HST*/ACS filters) centered at the galaxy. We then perform background subtraction to each stamp image using PHOTUTILS (Bradley et al. 2022a). Next, we perform point spread function (PSF) matching to homogenize the spatial resolution across filters. We degrade the spatial resolution of the images to match the resolution of F444W filter, which has the lowest spatial resolution (see Table 1). For this, we generate the empirical PSFs of *HST*/ACS and *JWST*/NIRcam filters along with the convolution kernels using PHOTUTILS package (see Appendix C). The PSF matching is carried out by convolving the stamp images with the convolution kernels. After PSF matching, we register all the stamp images to a common spatial sampling of

$0\!\!''04$ per pixel. At the end, we have multiband stamp images with a size of $151{\times}151$ pixels for each galaxy in our sample.

3.3. *Constructing Photometric Data Cubes*

PIXEDFIT further processes the stamp images to produce photometric data cubes. First, it defines a galaxy's region of interest. For each galaxy, segmentation maps are first produced in all filters using SEP (Barbary 2016) and those maps are then merged together into a single map. In the segmentation process, we use same parameters for all filters as follows. We set the detection threshold (`thresh`), the number of thresholds for deblending (`deblend_nthresh`), and the minimum contrast ratio for deblending (`deblend_cont`) to be 2.0, 40, and 0.005, respectively.

In some cases, the merged segmentation map is larger than expected, as can be inferred from the maps of multiband fluxes. This can be caused by some factors, for example, an interference from neighboring objects that is not separated well by the deblending process. We visually inspect the merged segmentation map of each galaxy to find out this issue. To deal with this, we tweak the deblending parameters to get cleaner segmentation maps or ignore segmentation map in some filters that has this deblending issue, then merge them again.

Once the galaxy's region is defined, then the fluxes of pixels within the region are calculated. We use PHOTFLAM keyword in the header of the GRIZLI imaging data products to convert the pixel value into flux density in the units of erg s^{-1}cm^{-2}Å^{-1}. The data cubes are then stored into FITS files. Figure 2 shows examples of the maps of multiband fluxes of galaxies in three fields analyzed in this work. The color images shown in the leftmost panels are created using `Trilogy`[6] (Coe et al. 2012).

3.4. *Pixel binning*

The SEDs of pixels are usually noisy and might not providing sufficient constraint to the models if fitting is done to them. Therefore, we perform pixel binning using PIXEDFIT to optimize the signal-to-noise ratio (S/N) of the spatially resolved SEDs. Basically, this process bins neighboring pixels to achieve a certain S/N ratio threshold. The unique pixel binning scheme in PIXEDFIT, which takes into account the similarity in SED shape among pixels, allows for achieving a sufficient S/N ratio in multiple filters of interest while preserving important spatial information at pixel level. A detailed description

---

[4] https://cosmic-spring.github.io/earendel.html

[5] https://github.com/aabdurrouf/piXedfit

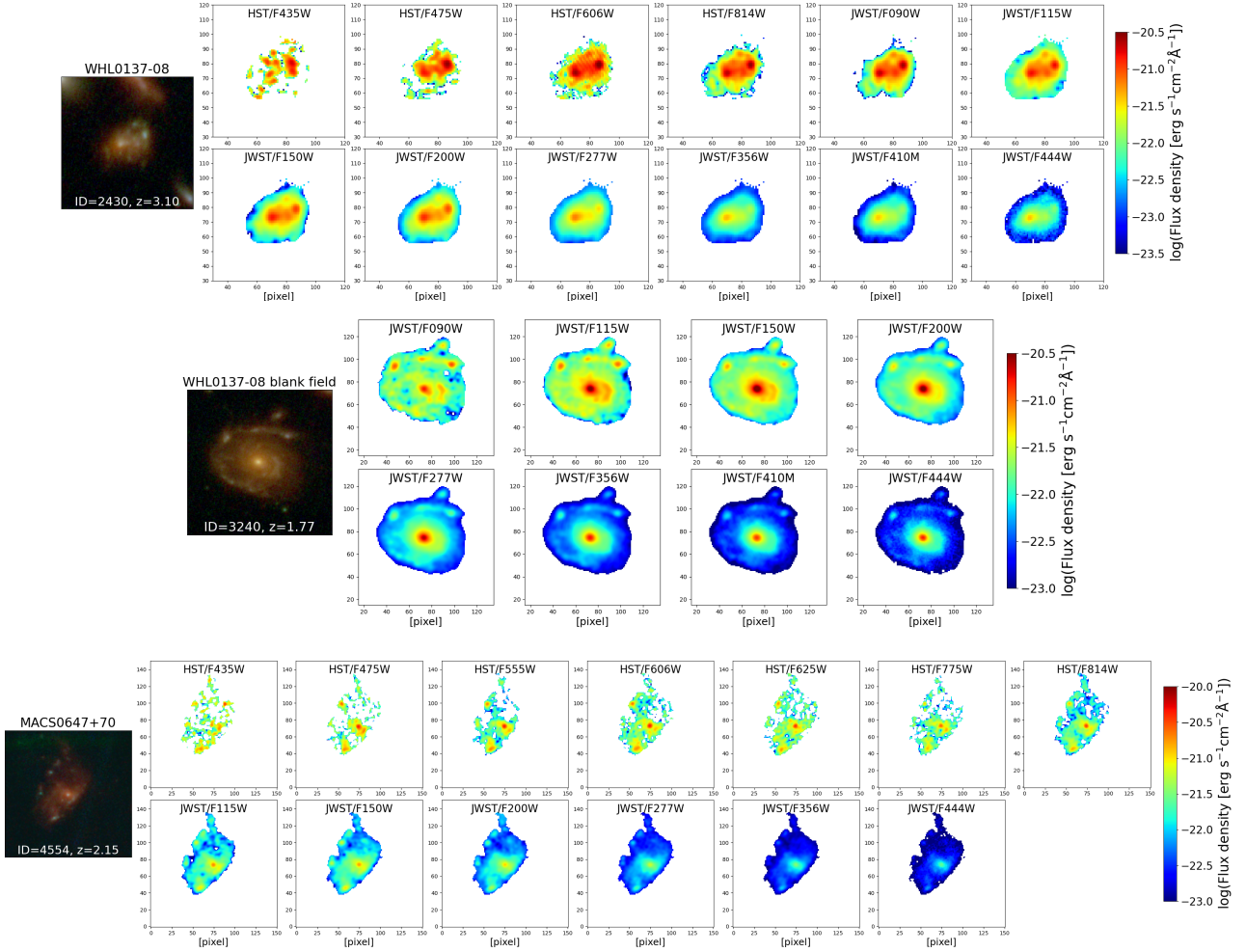[6] https://github.com/dancoe/trilogy

Figure 2. Examples of the maps of multiband fluxes produced from the image processing. Example of one galaxy is shown for each field, from top to bottom: WHL0137−08 cluster (observed in 12 filters), blank field (8 filters), and MACS0647+70 cluster (13 filters). The ID is based on our GRIZLI v4 public catalog.

of this pixel binning scheme can be seen in Abdurro'uf et al. (2021).

We assume the following parameters in the pixel binning process. We refer reader to Abdurro'uf et al. (2021) for more information about the parameters. We set S/N thresholds to 5 in all *JWST* NIRCam filters. We do not set S/N threshold to *HST* filters because the S/N ratio of pixels in the *HST* images are low, especially for galaxies at high redshifts. Setting a S/N threshold on the *HST* filters would put a strong constraint in the pixel binning process which can produce a coarser binning map and loosing important spatial information from the original images.

The rest of the binning parameters are as follows. We set a minimum diameter of 7 pixels, which is larger than the PSF FWHM size of our data cubes, a reduced χ^2 limit of 5 in the evaluation of the similarity of SED shape. We refer to F277W flux in determining the brightest pixel to be the center of a spatial bin. We

store new data cubes produced from this pixel binning process into FITS files. The total number of spatial bins in our sample galaxies is 24999. Figure 3 shows examples of the pixel binning maps produced from this process.

3.5. *Spatially Resolved SED Fitting*

Once we have the binned data cubes, we perform SED fitting to the SEDs of individual spatial bins in our sample galaxies. Here we use the SED fitting module in PIXEDFIT. The SED fitting in PIXEDFIT uses fully Bayesian technique. We refer reader to Abdurro'uf et al. (2021) for a detailed description of the SED modeling and fitting methods as well as comprehensive tests of its capabilities. In Appendix A, we perform SED-fitting tests using mock SEDs to demonstrate the robustness of our SED fitting method on the combined *HST* and *JWST* photometry. Moreover, in Appendix B we discuss how NIRCam photometry can potentially break the
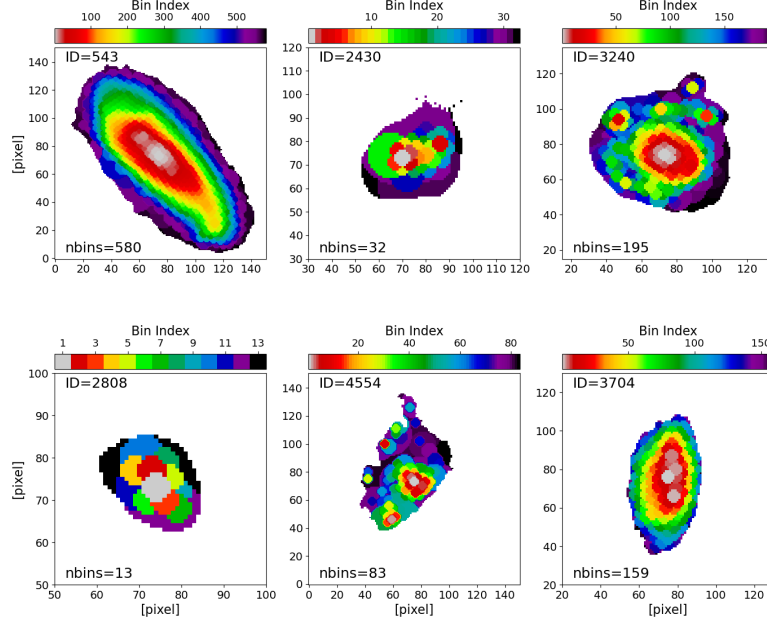
Figure 3. Examples of pixel binning results. The pixel binning process achieves a minimum S/N ratio of 5 in all *JWST* NIRCam filters.

Table 2. Free Parameters in the SED Modeling and the Assumed Priors.

Parameter	Description	Prior	Sampling/Scale
M_*	Stellar mass	Uniform: min= $\log(s_{\mathrm{best}}) - 2$, max= $\log(s_{\mathrm{best}}) + 2$[a]	Logarithmic
Z_*	Stellar metallicity	Uniform: min= $-2.0 + \log(Z_\odot)$, max= $0.2 + \log(Z_\odot)$	Logarithmic
t	Time since the onset of star formation ($\mathrm{age_{sys}}$) [b]	Uniform: min= -1.0, max = age of the universe at the galaxy's redshift[c]	Logarithmic
τ	Parameter that controls the peak time in the double power-law SFH model[b]	Uniform: min= -1.5, max= 1.14	Logarithmic
α	Parameter in the double power-law SFH model that controls the slope of the falling star formation episode[b]	Uniform: min= -2.0, max= 2.0	Logarithmic
β	Parameter in the double power-law SFH model that controls the slope of the rising star formation episode[b]	Uniform: min= -2.0, max= 2.0	Logarithmic
$\hat{\tau}_1$	Dust optical depth of the birth cloud in the Charlot & Fall (2000) dust attenuation law	Uniform: min= 0.0, max= 4.0	Linear
$\hat{\tau}_2$	Dust optical depth of the diffuse ISM in the Charlot & Fall (2000) dust attenuation law	Uniform: min= 0.0, max= 4.0	Linear
n	Power law index in the Charlot & Fall (2000) dust attenuation law	Uniform: min= -2.2, max= 0.4	Linear

NOTE— [a]s_{best} is the normalization of model SED derived from the initial fitting with the χ^2 minimization method (see Section 4.2.1 in Abdurro'uf et al. 2021). [b]The mathematical form of the double power-law SFH is given in Abdurro'uf et al. (2021, Equation 7 therein). [c]The redshift here is $z = z_{\mathrm{eazy}} - 0.3$ with z_{eazy} is the photometric redshift from the GRIZLI catalog which is derived using EAZYPY code. Subtraction by 0.3 is made to enlarge the range of t and account for the photometric redshift uncertainty.

degeneracies among age, dust, and metallicity in the SED fitting. In the following, we provide a brief description of the method and some assumptions applied in our SED fitting.

We use the Flexible Stellar Population Synthesis code (FSPS; Conroy et al. 2009; Conroy & Gunn 2010). It includes the nebular emission modeling that uses the CLOUDY code (Ferland et al. 1998, 2013). In this work, we assume the Chabrier (2003) initial mass function (IMF), Padova isochrones (Girardi et al. 2000; Marigo & Girardi 2007; Marigo et al. 2008), and MILES stellar spectral library (Sánchez-Blázquez et al. 2006; Falcón-Barroso et al. 2011). For the star formation history model, we assume an analytic model in the form of double power-law. It has been shown in Abdurro'uf et al. (2021) that this SFH form can give robust estimates of the stellar population properties and even SFH of galaxies, as tested using synthetic SEDs of simulated galaxies in the IllustrisTNG simulations. For simulating the effect of dust attenuation, we use the two-component dust attenuation law of Charlot & Fall (2000). This dust attenuation law gives an extra attenuation to stars younger than 10 Myr that are assumed to be residing in the dense molecular clouds, in addition to standard attenuation in the diffuse ISM. We model the attenuation due to intergalactic medium using Inoue et al. (2014) model. Since we do not have photometry that cover the rest-frames mid-infrared (MIR) and far-infrared (FIR), we switch off the modeling for dust emission and AGN dusty torus emission in the analysis throughout this work. The SED modeling has 9 free parameters. We summarize these parameters along with the assumed priors in Table 2. We assume a constant ionization parameter (U) of 0.01 in the modeling of the nebular emission.

In the current analysis, we rely on photometric redshift for all of galaxies in our sample because we do not have spectroscopic observations at the moment we carry out this analysis. To get redshift estimates of the galaxies, we perform SED fitting with piXedfit in which redshift is let to be free in the fitting. For this, we fit integrated SED within the effective radius of the galaxies. The effective radius is measured in F444W image using GALFIT(Peng et al. 2002, ;see Section 4.2). This is performed to get SEDs with high S/N while reducing contamination from noisy SEDs of pixels in the outskirt regions. In this fitting, we apply a prior on redshift in the form of a Gaussian function centered at the photometric redshift estimated by the EAZYPY taken from the GRIZLI catalog (see Section 3.1). We set a width of 0.5 for this Gaussian prior. This fitting is performed to derive redshift only. We then use this redshift information for the SED fitting of all spatial bins in the galaxy, in which we fix the redshift. We apply the Markov Chain Monte Carlo (MCMC) method in piXedfit. In the SED fitting for determining redshifts, we set the number of walkers to 100 and the number of steps per walker to 1000. For the SED fitting of spatial bins, we use 100 walkers and less number of steps (600) per walker for reducing computational time.

We show examples of SED fitting results of two galaxies in Figure 4, one galaxy from the WHL0137−08 cluster field (top panel) and the other galaxy from the blank field (bottom panel). For each galaxy, we show best-fit SEDs in the top right panel. The observed and best-fit photometric SEDs are shown with square and circle symbols, respectively. The SED in black is for the integrated within the effective radius, while those in other colors are for 5 examples of spatial bins in the galaxies. The corner plot in the lower left side shows the posterior probability distribution functions (PPDF) of the model parameters obtained from the fitting on the integrated SED within the effective radius. Above this corner plot, we show the PDFs of M_* and SFR of the spatial bins which the best-fit SEDs are shown in the top right panel. The best-fit spectra shown in the plot are drawn from the MCMC sampler chains, which distributions reflect the PPDF. Therefore, it is possible to get a slight shift in wavelength between the best-fit spectra of the central SED (where z is free in the fitting) and that of the spatial bins (where z is fixed in the fitting). This wavelength shift reflects the uncertainty of the estimated redshift. Finally, in the bottom right panel we show the maps of stellar population properties, including the M_* surface density (Σ_*), SFR surface density (Σ_{SFR}), mass-weighted age, $A_{V,1}$ ($1.086 \times \hat{\tau}_1$), $A_{V,2}$ ($1.086 \times \hat{\tau}_2$), and metallicity.

3.6. Lens Modeling

To estimate the magnifications due to the gravitational lensing effect by the clusters, we use the lens models constructed by our team. For the WHL0137−08 cluster, we use the same lens models that were used for analyzing the Earendel and the Sunrise Arc in Welch et al. (2022a), which were made publicly available[7]. These lens models were generated using four independent lens modeling software packages: Light-Traces-Mass (LTM, Zitrin et al. 2009, 2015; Broadhurst et al. 2005), Glafic (Oguri 2010), WSLAP (Diego et al. 2005, 2007), and Lenstool (Kneib et al. 1993; Jullo et al. 2007; Jullo & Kneib 2009). Please see Welch et al. (2022a) for detailed information about each model. Sample galax-

---

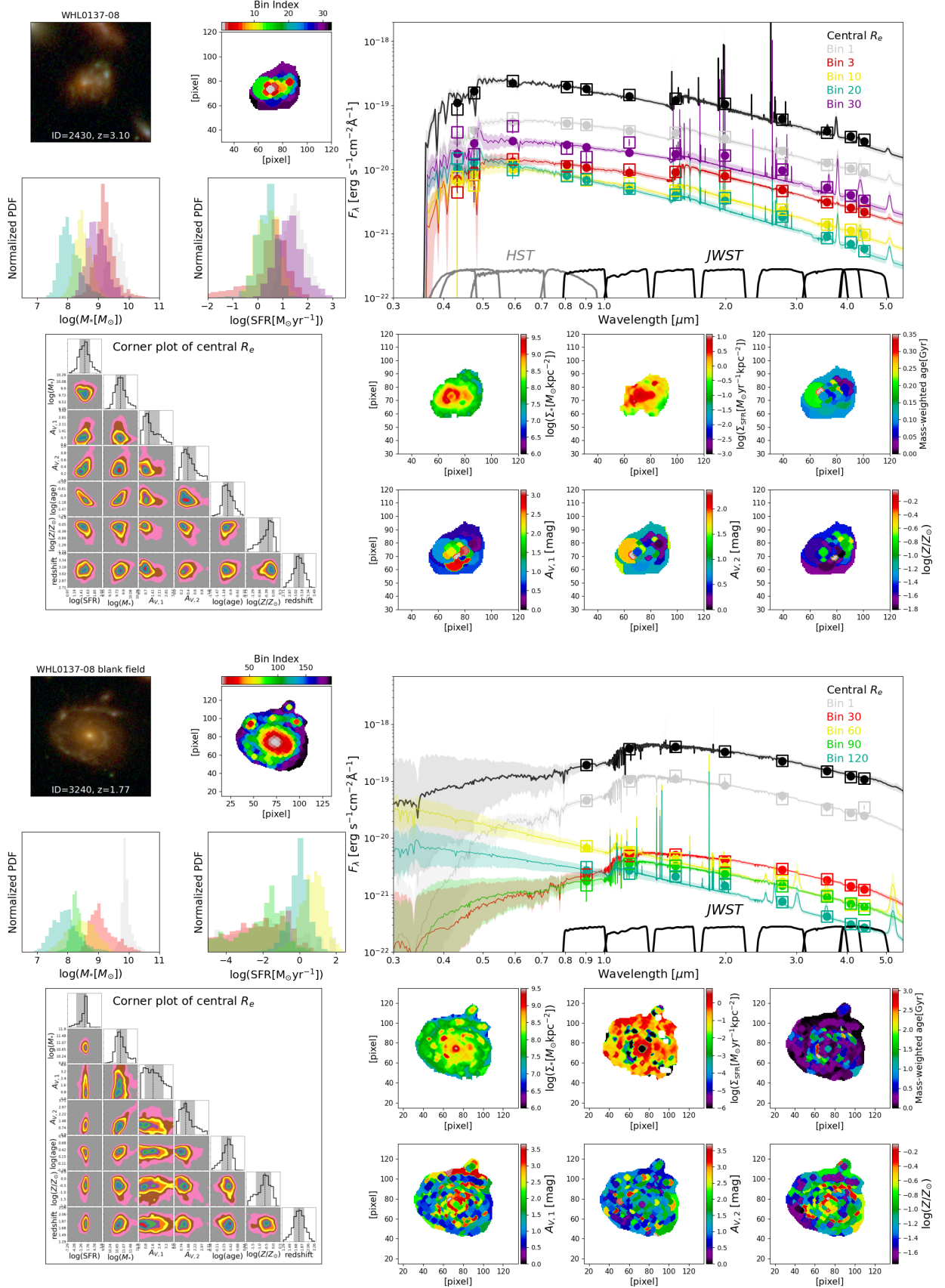[7] https://relics.stsci.edu/lens_models/outgoing/whl0137-08/

Figure 4. Examples of SED fits of a galaxy in the WHL0137−08 cluster (top panel) and the blank field (bottom panel). The SED plots show the best-fit SEDs from the fitting to integrated SED within the effective radius (black color) and 5 examples of spatial bins (in colors). The corner plots show the posterior probability distributions of the parameters obtained from fitting to the central integrated SED. Above this corner plots, we show PDFs of M_* and SFR of the five spatial bins. Finally, the maps of stellar population properties derived from this analysis are shown in the bottom right corner.

ies located in the blank field are expected to have only weak magnifications of $\mu \lesssim 1.1$. With the multiple lens models available for this cluster, we estimate the total and tangential (i.e., linear) magnifications (μ and μ_t, respectively) of each galaxy by taking the average values. By this way, we account for the modeling uncertainties. Based on the standard deviation values, we find that the magnifications do not vary a lot among the models. The median standard deviations of μ and μ_t are 0.11 and 0.10 dex, respectively.

The lens models for MACS0647+70 cluster have been constructed in the past using the *HST* imaging data. The first lens model for MACS0647+70, before the CLASH survey, was provided by Zitrin et al. (2011) using `LTM` method. With the addition of *HST* imaging data from CLASH, new lens models were established using various methods, including `Lenstool`, `LTM`, `WSLAP`, and `LensPerfect` (Coe et al. 2008). These lens models have been used in previous studies in CLASH (e.g., Coe et al. 2013; Zitrin et al. 2015; Chan et al. 2017). Now with the addition of *JWST* NIRCam imaging data, which add on many new strongly-lensed multiple-image candidates (thanks to its high spatial resolution and depth), a new lens model has been established using the `dPIEeNFW` method (Zitrin et al. 2015) with some modifications. A detailed information on this lens modeling of MACS0647+70 cluster along with the list of the multiple-image systems are given in Meena et al. (2022). This new method has also been implemented to several clusters using *JWST* NIRCam data (Pascale et al. 2022; Roberts-Borsani et al. 2022; Hsiao et al. 2022; Williams et al. 2022). We used this lens model constructed by Meena et al. (2022) for galaxies in the MACS0647+70 field. We correct the M_* and SFR obtained from SED fitting for the lensing magnification by dividing them with μ. We also correct size or radius measurement (e.g. half-mass and half-SFR radii; see Section 4.3) by dividing them with μ_t.

4. RESULTS

4.1. *Integrated Properties*

Before analyzing the spatially resolved properties of our sample galaxies, we first present their integrated (i.e., global) properties. To bring it into the context of the global demographics of galaxies, we plot our sample on the integrated star-forming main sequence (SFMS) diagram, as shown in the left panel of Figure 5. The integrated M_* and SFR of a galaxy are derived by summing up the values in pixels obtained from the spatially resolved SED fitting. Due to our limited sample, we plot all our galaxies on the SFMS diagram instead of dividing them into a number of redshift bins and ex-

amine the SFMS relation in each bin. This can cause the broad distribution as shown in the figure. Different symbols represent the fields where the galaxies are located (WHL0137$-$08, blank field, and MACS0647+70), whereas color-coding represent redshift grouping, where we divide the redshift range into five bins. The dashed lines show the SFMS relations at the median redshifts of the five redshift bins, calculated using the prescription from Speagle et al. (2014). The lines are colored based on the redshift groups.

We then classify our sample galaxies into star-forming, green valley, and quiescent groups based on their positions with respect to the SFMS ridge line at the redshift of the galaxies. We define star-forming, green-valley, and quiescent galaxies as those having SFR $>$ $\text{SFR}_{\text{MS}}(z, M_*) - 0.4$ dex, $\text{SFR}_{\text{MS}}(z, M_*) - 0.4 \geq \text{SFR} >$ $\text{SFR}_{\text{MS}}(z, M_*) - 1.0$ dex, and SFR $\leq \text{SFR}_{\text{MS}}(z, M_*) - 1.0$ dex, respectively, where $\text{SFR}_{\text{MS}}(z, M_*)$ is the SFMS ridge line for exact z and M_* of the individual galaxies. With this selection criteria, we have 219, 108, and 117 total numbers of the star-forming, green-valley, and quiescent galaxies from the three fields, respectively. We will use these classified samples throughout the analysis in this paper to investigate the differences in spatially resolved properties of galaxies in various evolutionary stages. The right panel of Figure 5 show the distributions of these groups on the SFMS diagram.

To get a sense of how the global specific SFR (sSFR$\equiv$ SFR/M_*) evolves with cosmic time in our sample galaxies, we plot the sSFR against redshift in Figure 6. We can see a clear trend of decreasing global sSFR with cosmic time and an increasing number of quiescent galaxies along the way. In our sample, quiescent galaxies start to emerge from $z \sim 3$, ~ 2 Gyr after the Big Bang. To compare our global sSFR trend with the similar trend from previous studies, we plot sSFR(z) inferred from the SFMS normalization based on Speagle et al. (2014) prescription. We calculate sSFR(z) for four M_* of $10^{8.5}$, 10^{10}, 10^{11}, and 10^{12} $M_\odot$ and show them in the figure as black dashed lines. We see an overall agreement between the evolutionary trend of sSFR in our sample and that expected based on the evolution of the SFMS normalization from Speagle et al. (2014). We also show global sSFR measurements of $z \sim 0$ spiral galaxies from Abdurro'uf & Akiyama (2017) and Abdurro'uf et al. (2022a) (personal communication) who performed spatially resolved SED fitting using PIXEDFIT.

Previous studies have classified passive galaxies using various methods. One of the methods is by comparing the Hubble time (t_H) with the mass doubling time (i.e., inverse of sSFR). Basically, this method defines quiescent galaxies as those having sSFR $< 1/t_H$. The red
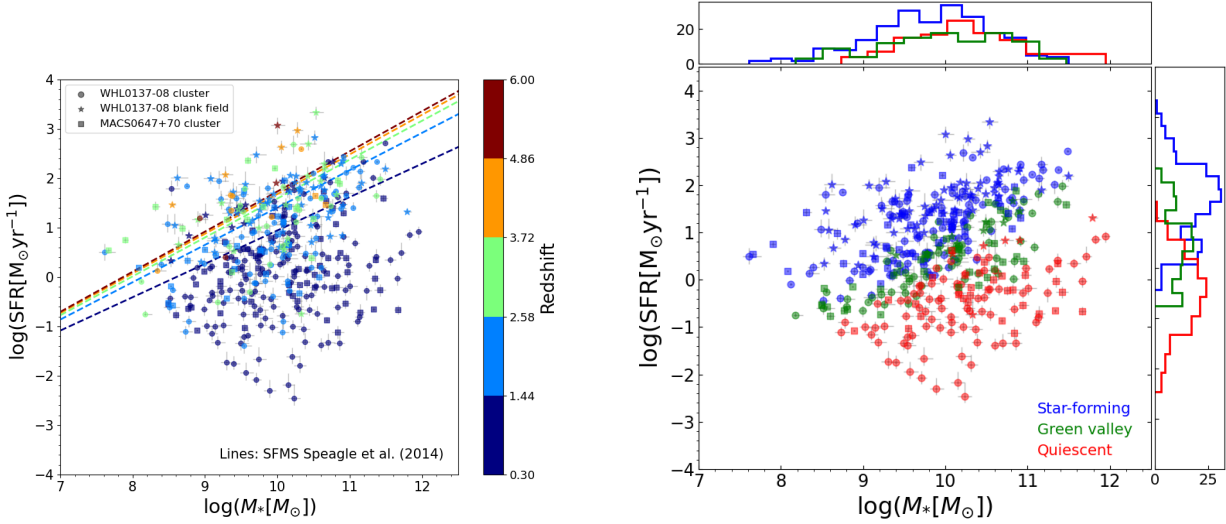
Figure 5. *Left panel*: Integrated (i.e., global) M_* and SFR of our sample galaxies. Different symbols represent different fields where the galaxies are located, whereas the color-coding represents redshift grouping. The dashed lines show the global SFMS relations at the median redshifts of the 5 redshift groups calculated using the prescription from Speagle et al. (2014). The lines are colored based on the redshift groups. *Right panel*: Distribution the star-forming, green-valley, and quiescent galaxies in our sample that are classified as having $\mathrm{SFR} > \mathrm{SFR_{MS}}(z, M_*) - 0.4$ dex, $\mathrm{SFR_{MS}}(z, M_*) - 0.4 \geq \mathrm{SFR} > \mathrm{SFR_{MS}}(z, M_*) - 1.0$ dex, and $\mathrm{SFR} \leq \mathrm{SFR_{MS}}(z, M_*) - 1.0$ dex, respectively. $\mathrm{SFR_{MS}}(z, M_*)$ is the SFMS ridge line that is calculated for exact z and M_* of the individual galaxies.

dashed line in Figure 6 represents $1/t_H$. To compare our quiescent classification with this method, we plot $1/t_H$ in Figure 6, which is shown with red dashed line. We can see that our quiescent galaxies lie below this line, indicating that our classification method is consistent with that based on t_H.

4.2. *Radial Profiles of the Stellar Population Properties*

As we have shown the global properties of the sample galaxies and classified them into star-forming, green-valley, and quiescent groups, now we will analyze their spatially resolved properties. We start by presenting the radial profiles of the stellar population properties to get a sense of how the properties vary radially within the galaxies. To derive the radial profiles, first, we perform 2D single-component Sérsic fitting using GALFIT (Peng et al. 2002) on F444W stamp image of each galaxy to get their ellipticities, position angles, and central coordinates. We then use this information to define elliptical annuli in the radial profile calculation. The radial profiles are derived from the 2D maps of properties obtained from the spatially resolved SED fitting by averaging values of pixels within the annuli. Since galaxies have a wide range of size, we normalize the radius by the half-mass radius (R_e), which is the radius that covers half of the integrated M_*. We use radial increment (δr)
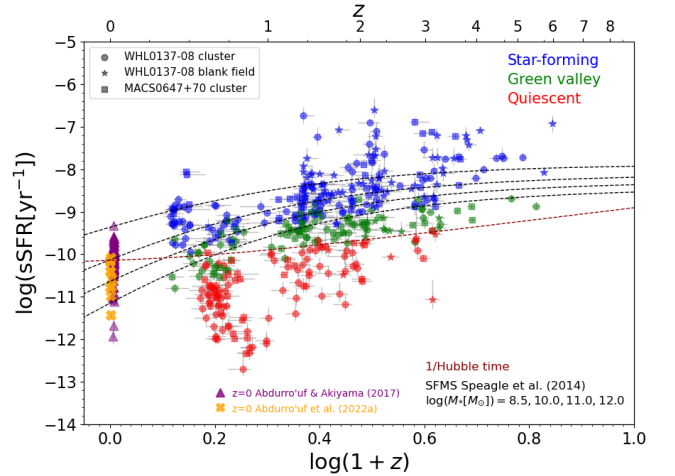

Figure 6. Evolution of the integrated specific SFR (sSFR) with redshift. The black dashed lines represent sSFR evolution of SFMS galaxies with $M_* = 10^{8.5}$, 10^{10}, 10^{11}, and 10^{12} $M_\odot$ (decreasing normalization) as inferred from the normalization of the SFMS, calculated using the prescription from Speagle et al. (2014). The red dashed line represents $1/t_H$ where t_H is the Hubble time. Almost all our quiescent galaxies lie below this line, indicating that their mass doubling timescale is longer than t_H.

of $0.3R_e$. Thanks to the gravitational lensing effect, we

can resolve many of our galaxies down to sub-kpc scales (109 galaxies in our sample have delensed $R_e < 1$ kpc).

Figure 7 shows the radial profiles of the stellar mass surface density (Σ_*). We divide the sample into 5 bins of redshift and 4 bins of M_* to see how the radial profiles vary with global M_* and cosmic time. Moreover, we indicate the star-forming, green valley, and quiescent galaxies with different colors, in a similar way as in Figure 6. For groups that contain at least 5 galaxies, we show average radial profiles with tick line. Some interesting trends from Figure 7 is that at each redshift bin, more massive galaxies tend to have higher $\Sigma_*(r)$ normalization than less massive galaxies, indicating that the excess in mass happens across the entire radius. Moreover, we also see that quiescent galaxies tend to have higher $\Sigma_*(r)$ normalization than the star-forming and green-valley galaxies in all redshift. This is especially clear in the most massive groups. It is also interesting to see that $\Sigma_*(r)$ profiles have negative gradient (i.e., decreasing mass with increasing radius) in all redshift and mass bins, although the profiles seem to be shallower at higher redshifts.

To see how galaxies quench their star formation, specifically where in the galaxies the suppression of star formation first happens and how it progresses over cosmic time, next we analyze the radial profiles of sSFR. The radial profiles of sSFR are shown in Figure 8. As we can see from this figure, the sSFR radial profiles of the majority of our sample galaxies at $z \gtrsim 2.5$ are broadly flat, while they show more diversity in shape at lower redshifts. At $0.8 \lesssim z \lesssim 2.5$, star-forming galaxies in our sample tend to have a flat or centrally-peaked sSFR(r), while quiescent galaxies tend to have centrally-suppressed sSFR(r). On the other hand, green-valley galaxies in our sample seem to have broadly flat radial profile up to $z \sim 1.0$, except in the most massive group, where some of them show a sSFR suppression in their central regions. At lower redshifts, the majority of our sample galaxies have centrally-suppressed sSFR(r). It is also interesting to see that the majority of star-forming galaxies at $0.8 \lesssim z \lesssim 2.5$ (in which the cosmic noon epoch is covered), have a centrally-peaked sSFR(r). This central elevation of sSFR is not observed at higher redshifts, instead they have roughly flat radial profiles.

Next, we analyze the radial profiles of the stellar population age to see how this quantity varies radially within our sample galaxies and investigate the underlying stellar population properties causing the diversity in the sSFR radial profiles. From our spatially resolved SED fitting, we obtain maps of the mass-weighted ages, which is the average age of stars in a stellar population as weighted by the stellar mass formed over the course of the star formation history. The age radial profiles are shown in Figure 9. As can be seen from this figure, there is a trend of increasing overall age of the stellar populations in galaxies over cosmic time, as indicated by the increasing normalization of the radial profiles with decreasing redshift. The star-forming galaxies that have a centrally-peaked sSFR(r) at $0.8 \lesssim z \lesssim 2.5$ (possibly around the cosmic noon epoch) as shown in Figure 8 are likely in a phase of rapid star formation in their centers (i.e., a nuclear starburst; e.g., Dekel & Burkert 2014; Zolotov et al. 2015; Tacchella et al. 2016b), as indicated by the young stellar populations (age $\lesssim 100$ Myr) in their central regions. At this epoch, green-valley and quiescent galaxies tend to have radially decreasing age profiles (i.e., negative gradient). At $0.3 < z < 0.8$, low-mass galaxies ($\log(M_*/M_\odot) < 9.5$) in all stages of star formation have radially decreasing age radial profiles (i.e., negative gradient). A similar trend is still hold for star-forming and green-valley galaxies in higher mass group ($9.5 < \log(M_*/M_\odot) < 10.5$). On the other hand, quiescent galaxies at this epoch tend to have overall flat and old stellar populations across their entire radial extents, with higher normalization (i.e., older) than that of star-forming and quiescent galaxies.

4.3. Compactness of the Spatial Distributions of Stellar Mass and SFR

The centrally-peaked sSFR(r) of star-forming galaxies at around the cosmic noon epoch indicates that they are likely undergoing a nuclear starburst that builds the bulge component. The centrally-suppressed sSFR(r) profiles which start to emerge in quiescent galaxies at around the same epoch can be caused by the cessation of star formation in the center and/or a matured bulge that has been formed in these galaxies. This trend provides a hint on how galaxies quench their star formation, which seems to progress in an inside-to-outside manner (i.e., quenching starts from the center and then propagates outward). At the same time, this trends may indicate that galaxies build their central regions first, forming a mature bulge, and then subsequently assemble their disk through star formation (i.e., inside-out growth). To further investigate this, next we compare the compactness of the spatial distributions of M_* and SFR by means of the half-mass and half-SFR radii.

We compare the half-mass radius and the half-SFR radius in Figure 10. The half-SFR radius is a radius (measured along the elliptical semi-major axis) that covers half of the total SFR. Similar as in Figure 6, the star-forming, green-valley, and quiescent galaxies are shown in blue, green, and red colors, respectively. To com-
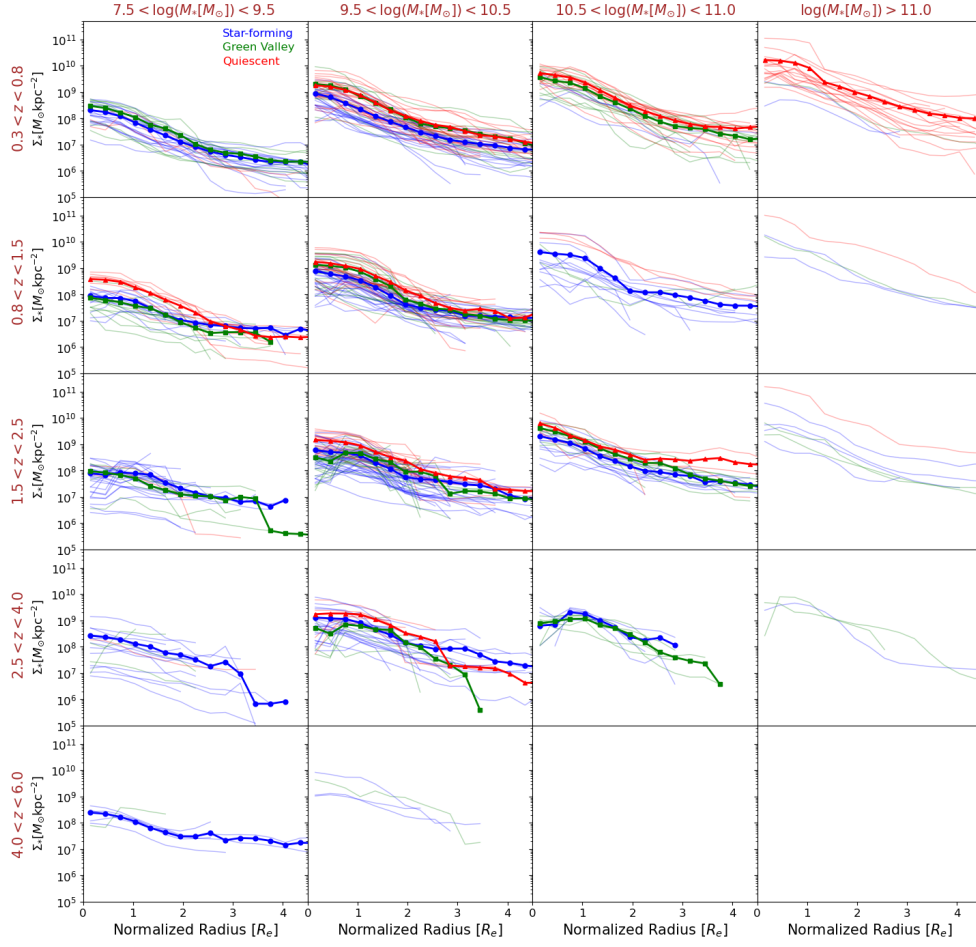
Figure 7. Radial profiles of the stellar mass surface density (Σ_*). The sample galaxies are divided into 4 bins of global M_* and 5 bins of redshift. At each group, we further classify the galaxies into star-forming, green-valley, and quiescent groups and indicate them with different colors. For sub-groups that contain at least 5 galaxies, we show average radial profiles with tick line. At each redshift bin, more massive galaxies tend to have higher $\Sigma_*(r)$ normalization than less massive galaxies, indicating that the excess in mass happens across the galaxy region. Quiescent galaxies tend to have higher $\Sigma_*(r)$ normalization than star-forming in all redshifts. This is especially clear in high M_* bins.

pare the distributions of our star-forming and quiescent galaxies on this diagram, we plot the density contours. As can be seen from this figure, star-forming galaxies broadly follow the one-to-one line, whereas quiescent galaxies are excess above the line. This means that in quiescent galaxies, the spatial distribution of SFR is more extended than that of stellar mass, indicating that star formation is on-going in the disk and less active in the central region. It is also possible that a massive bulge might has been formed in the centers, making a more compact stellar mass distribution. On the other hand, star-forming galaxies are equally distributed. Some star-forming galaxies have spatially more compact star formation distribution than the stellar mass (i.e., below the one-to-one line), which indicates

that active star-formation happens at their centers. On the other hand, in the star-forming galaxies that have extended star formation (i.e., above the one-to-one line), the bulge might has been built and active star formation is now progressing outward and building the disk.

It has been known that galaxy size correlates with global M_* for galaxies out to at least $z \sim 3$ (i.e., the size–mass relation; e.g., Shen et al. 2003; van der Wel et al. 2014; Morishita et al. 2014; Yang et al. 2021). However, most of the previous studies rely on galaxy half-light radii as a measure of galaxy size. Since mass-to-light ratios are not constant across a galaxy's region, but instead has a gradient, the half-light radii are not a direct probe of the underlying stellar mass profiles. Therefore, it is expected that the half-mass and half-
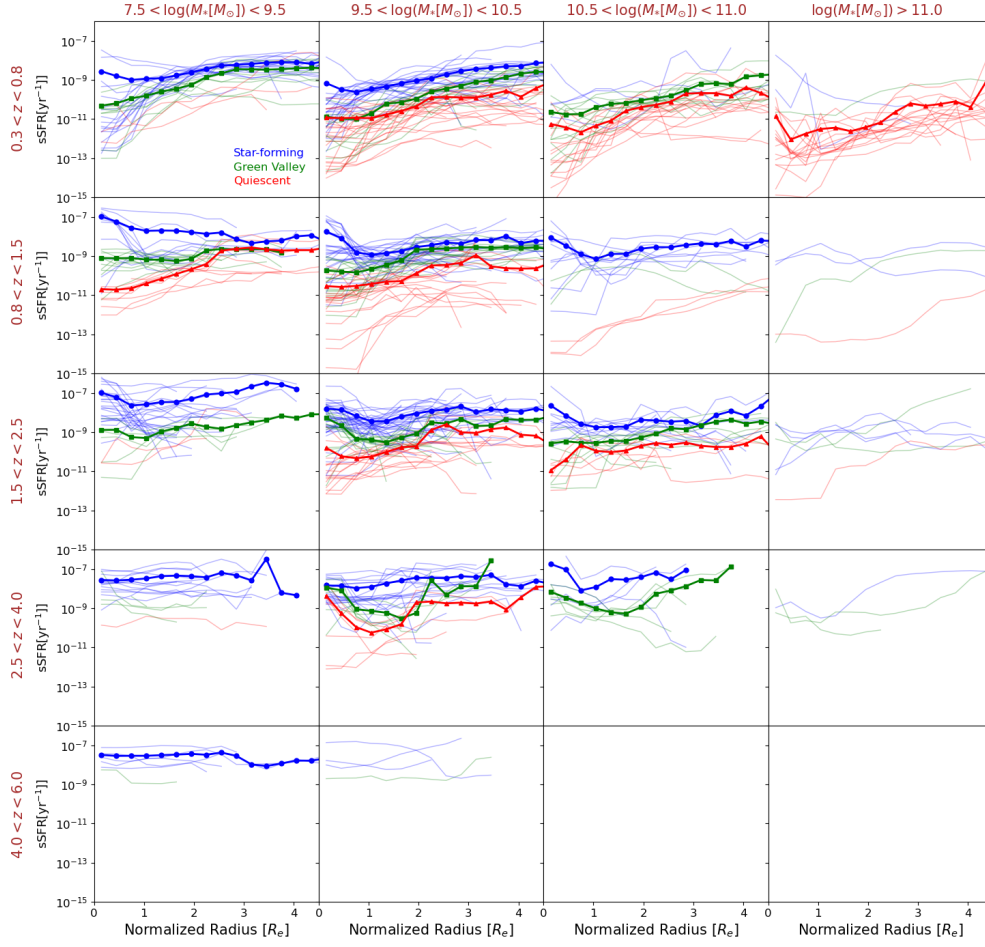
Figure 8. Similar to Figure 7 but for radial profiles of sSFR. At $z \gtrsim 2.5$, our sample galaxies tend to have a broadly flat sSFR(r), while at the lower redshifts they show more diversity in shape. At $0.8 \lesssim z \lesssim 2.5$, the majority of star-forming galaxies have an elevation of sSFR in their central regions, while they tend to have centrally-suppressed sSFR radial profiles at lower redshifts. On the other hand, quiescent galaxies in our sample tend to have centrally-suppressed sSFR radial profiles since $z \sim 1.5$.

light radii are different. The difference in size as probed by light and mass profiles in galaxies out to at least $z \sim 2.5$ has been investigated by previous studies (e.g., Suess et al. 2019).

Now, we check how half-mass and half-SFR radii correlate with integrated M_* in our sample galaxies. We show the correlations in Figure 11. Overall, we see that both half-mass and half-SFR radii increase as increasing integrated M_*. However, we observe a difference in how star-forming and quiescent galaxies are distributed in the two correlations. In the top panel, we can see that star-forming galaxies tend to have larger half-mass radius than quiescent galaxies in all masses. On the other hand, as can be seen from the bottom panel, there is no clear difference between the star-forming and quiescent galaxies in terms of the half-SFR radius, although star-

forming galaxies tend to have wider range of half-SFR radius than quiescent galaxies.

In agreement with the trend we observe here, previous studies using half-light radii also found that star-forming galaxies are larger than quiescent galaxies in all M_* (van der Wel et al. 2014). However, when the half-mass radius is used, the normalization of the relation decreases and the slope as well become shallower (Suess et al. 2019). We do not intend to measure the slope and normalization of the size–mass relations we observe here because of the limited sample we have in the current study. Ideally we need a large sample of galaxies and divide them into some redshift bins. In this work, we combine all galaxies in our sample despite the fact that they are located in a wide range of redshift.
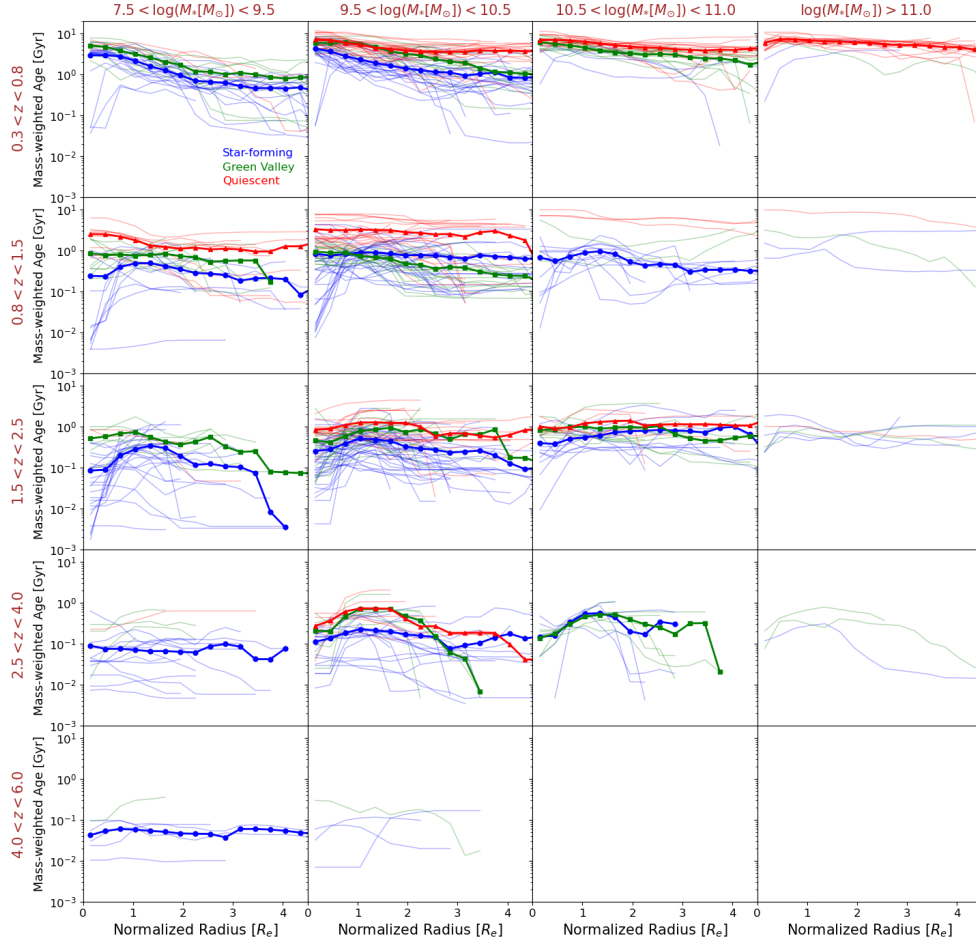
Figure 9. Similar to Figure 7 but for radial profiles of the stellar population age. There is a trend of increasing overall age of the stellar populations in galaxies over cosmic time. At $0.8 \lesssim z \lesssim 2.5$ (possibly around the cosmic noon epoch), a large fraction of our star-forming galaxies have a centrally-suppressed age radial profile. Those galaxies have centrally-peaked sSFR radial profiles as shown in Figure 8. These trends indicate that they are likely to have an on-going nuclear starburst event.

4.4. *Central Stellar Mass Surface Density*

We have observed that quiescent galaxies have smaller half-mass radius than the star-forming galaxies. The quiescent galaxies at $z \lesssim 2.5$ also have centrally-suppressed sSFR radial profiles. The compactness of quiescent galaxies can be caused by the massive bulge that have been formed in their centers. This massive bulge may also be the reason behind the central suppression of sSFR. Therefore, here we investigate the stellar mass surface density in the central 1 kpc radius ($\Sigma_{*,1\mathrm{kpc}}$) of our sample galaxies.

Figure 12 shows a relationship between the integrated M_* and $\Sigma_{*,1\mathrm{kpc}}$. A tight relationship is evidenced from this figure, which indicates that $\Sigma_{*,1\mathrm{kpc}}$ grows hand-in-hand with the integrated M_* of the galaxies. We fit the relation involving all galaxies in our sample with a linear function (in logarithmic scale) using the Orthogonal

Distance Regression (ODR) method and find that the relation has a scatter of 0.38 dex. The best-fit linear function (with slope = 1.10 and zero-point = −2.33) is shown with the purple dashed line. It is interesting to see that quiescent galaxies mostly reside in a tight locus at the top of the relation. This trend indicates that quiescent galaxies are tend to be massive and have a massive central stellar mass density, perhaps associated with a bulge that has been formed in these galaxies. This massive central component might in part causes the more compact (i.e., smaller half-mass radius) size of quiescent galaxies compared to the star-forming galaxies. In Section 5.1, we will discuss further how this central stellar mass density evolves with redshift and correlates with star formation in the inner and outer regions of the galaxies.
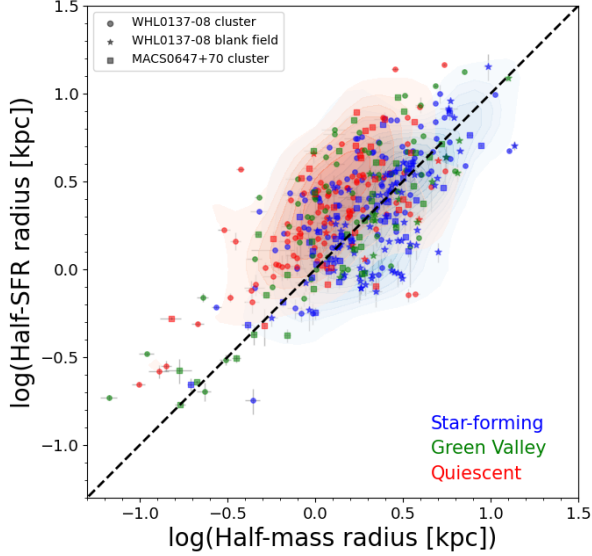
Figure 10. Comparison between the half-mass radius and half-SFR radius. The overall symbols in this figure are the same as those in Figure 6. The red and blue contours show the number densities of the star-forming and quiescent galaxies. The majority of quiescent galaxies in our sample have spatially more extended star formation distribution than the stellar mass. Star-forming galaxies are equally distributed on the diagram. In star-forming galaxies with compact SFR distribution (i.e., below the one-to-one line), an active star formation happen in the central region. On the other hand, in star-forming galaxies with less compact SFR distribution, a bulge might might have been built and active star formation is now progressing outward, building the disk.

A similar relationship has also been observed by previous studies in galaxies at $z \lesssim 3$ (e.g., Fang et al. 2013; Tacchella et al. 2015; Barro et al. 2017). Using a larger sample than ours, they also found that quiescent galaxies occupy a tight locus on top of the overall relation with all galaxies. The relation involving only quiescent galaxies has a shallower slope than that with the star-forming galaxies only. The black and red dashed lines are the best-fit to the $M_*-\Sigma_{*,\mathrm{1kpc}}$ relation of $z \sim 0$ passive galaxies reported by Fang et al. (2013) and Tacchella et al. (2015), respectively, whereas the blue line is the best-fit to the relation of $z \sim 0$ star-forming galaxies from Tacchella et al. (2015). In our result, we also see a slight bending at the tip of the distribution of quiescent galaxies, as can be seen from the density contour. It is interesting to see the consistency between the $M_*-\Sigma_{*,\mathrm{1kpc}}$ relation from our study and that from the literature despite the fact that our sample galaxies cover wider redshift range ($0.3 < z < 6.0$). It suggests that
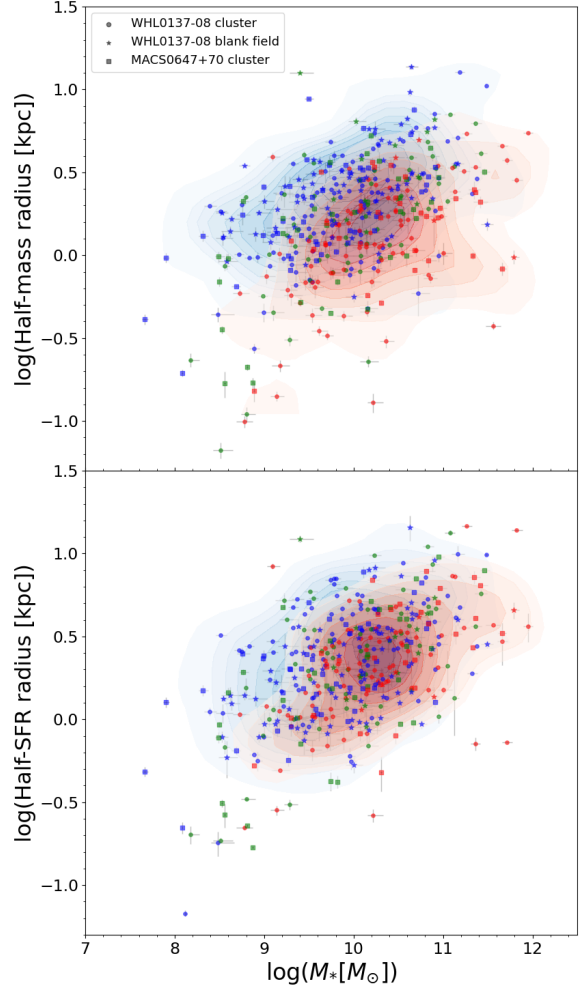
Figure 11. The half-mass (top panel) and half-SFR (bottom panel) radii as a function of integrated M_*. The overall symbols in this figure are the same as those in Figure 10. The half-mass radius is defined as the radius that covers half of the total M_*, while the half-SFR radius is the radius covering half of the total SFR. Both half-mass and half-SFR radii increase with increasing M_*. The M_* vs half-mass radius diagram shows that overall, the star-forming galaxies tend to have a larger size than quiescent galaxies. However, there is no clear difference between the two groups in terms of the size of the SFR distribution.

this relation is universal and galaxies evolve along this tight relation over cosmic time.

5. DISCUSSIONS

5.1. *How do Galaxies Grow and Quench Over Cosmic Time?*

In this section, we exploit our results to try to infer on how galaxies assemble their structures and eventually
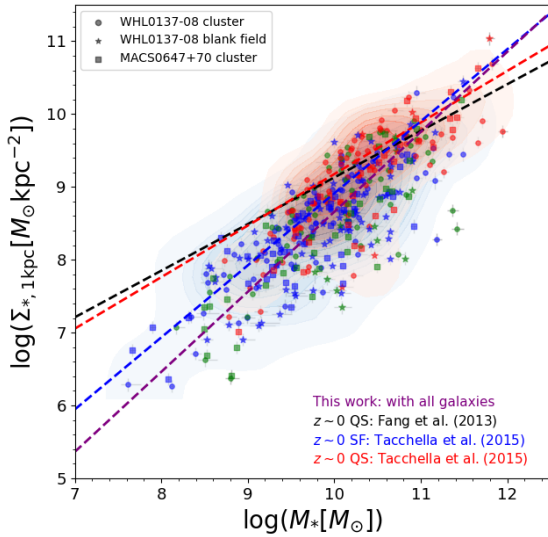
Figure 12. A tight relationship between the integrated M_* and stellar mass surface density within the central 1 kpc radius ($\Sigma_{*,1\mathrm{kpc}}$). The overall symbols in this figure is the same as those in Figure 10. This relation indicates that $\Sigma_{*,1\mathrm{kpc}}$ grows hand-in-hand with the integrated M_*. The quiescent galaxies mostly reside in the top locus of the relation, indicating that they are tend to be massive and have a massive spheroid in their centers. The purple dashed line is the best-fit linear function to our sample galaxies, which has slope $= 1.10$, zero-point $= -2.33$, and scatter of 0.38 dex. The black and red dashed lines are the best-fit to the same relation found in $z \sim 0$ passive galaxies reported by Fang et al. (2013) and Tacchella et al. (2015), respectively, whereas the blue line is the best-fit to the relation of $z \sim 0$ star-forming galaxies from Tacchella et al. (2015).

cease their star formation activities over the course of their life. In particular, we are interested to investigate how the processes of stellar mass buildup and quenching were propagating within the galaxies. Based on the models of the hierarchical galaxy formation paradigm, within the framework of the ΛCDM cosmology, galaxies are predicted to build their structures over cosmic time in an inside-out manner where the central component was built first and subsequently the disk structure is assembled gradually over time (e.g., Cole et al. 2000; van den Bosch 2002; Aumer & White 2013). This assembly process happens through the series of gas accretions via mergers and filamentary accretion through cosmic web.

In a gas-rich merger, gas can fall rapidly into the center of the gravitational potential, causing a compaction of gas that eventually triggers nuclear starburst event (e.g., Dekel & Burkert 2014). Other smoother gas streams can also lead to the central gas compaction, e.g., counter-rotating streams and low angular momen-

tum recycled gas. Based on the zoom-in cosmological hydrodynamical simulations, this wet compaction event is predicted to typically occur in $\sim 10^{9.5} M_{\odot}$ galaxies at $z \sim 2-4$ (e.g., Zolotov et al. 2015; Tacchella et al. 2016b,a). During this event, the star formation at the center is very intense, which converts massive gas concentration rapidly into stars (i.e., with short depletion time). This process depletes the gas in galaxies and make SFR to decline. However, the gas compaction event can occur multiple times in the high redshift galaxies, causing an up-and-down of their SFRs. This could appear as an oscillation around the SFMS-ridge line. The gas compaction and nuclear starburst processes can build the massive bulge in the centers of the galaxies (Tacchella et al. 2016b,a). Subsequently, galaxies can reach full quenching when the timescale of gas replenishment in the disk is longer than the timescale of gas depletion by star formation. This is more likely happen at lower redshifts, when the cosmological gas accretion rate is low, and especially so in a hot halo above the critical halo mass of $10^{11.5} M_{\odot}$ (Birnboim & Dekel 2003; Kereš et al. 2005; Dekel & Birnboim 2006). In general, an emerging picture from the above scenarios is that galaxies build their structures and quench their star formation in an inside-out manner.

Next, we will exploit our observational results to find indications of the above model predictions. We note that our current sample is limited, which may cause some biases in our interpretations. Moreover, more information from multiwavelength observations are needed for more comprehensive study on this, including maps of the gas mass and their kinematics which can be obtained from radio and integral field spectroscopy observations. We leave this for future works.

First, we examine the evolution of the ratio between the half-SFR and half-mass radii and the ratio between the sSFR in the inner (sSFR$_{\mathrm{in}}$) and outter (sSFR$_{\mathrm{out}}$) regions of the galaxies. We show the evolution of these quantities in Figure 13. The sSFR$_{\mathrm{in}}$ and sSFR$_{\mathrm{out}}$ are defined as the total sSFR inside and outside of the half-mass radius, respectively. In the study of galaxy evolution, we face the fact that we observe galaxies at a certain cosmic time. In other words, the galaxies across wide redshift that we observe here are not necessarily connected evolutionarily (i.e., they may not progenitor–descendant pairs), which makes it difficult to interpret an evolutionary trend from our study. Previous studies have tried to connect galaxies using a M_* growth function ($M_*(z)$) derived from the stellar mass function assuming a constant number density (e.g., van Dokkum et al. 2010, 2013). To try to connect galaxies in our sample and derive some evolutionary trends from their prop-

erties, we use $M_*(z)$ from van Dokkum et al. (2013) (Eq. 1 therein), which was designed for tracing the evolution of Milky Way analogs (i.e., having $M_* = 5 \times 10^{10} M_\odot$ at $z = 0$). We bin redshift with a width of 0.7. By using the $M_*(z)$ function, We then choose galaxies that fall within ± 0.35 dex in M_* at each redshift bin. Our model only extends up to $z = 4.5$ because there are no low mass galaxies selected beyond it in our sample. This can be caused by a bias in our sample selection (see Section 2.2). This toy empirical model is only intended for a reference in interpreting observational trends. We show evolutionary trends of this toy model with black diamond symbols. For comparison, we also show the trends observed in local spiral galaxies, as inferred from the data analyzed by Abdurro'uf & Akiyama (2017) and Abdurro'uf et al. (2022a) (personal communication).

The ratio between the half-SFR and half-mass radii $(R_{e,\mathrm{SFR}}/R_e)$ tells about the relative extent of the SFR distribution compared to the stellar mass distribution. A ratio $R_{e,\mathrm{SFR}}/R_e < 1$ implies a more compact SFR distribution than the stellar mass, whereas $R_{e,\mathrm{SFR}}/R_e > 1$ implies a more compact mass distribution than star formation. $R_{e,\mathrm{SFR}}/R_e << 1$ may indicate an on-going nuclear starburst, while $R_{e,\mathrm{SFR}}/R_e >> 1$ indicates that a massive bulge has been built in the galaxies. From Figure 13, we can see that from an early epoch up to $z \sim 3.5$, the two ratios are close to unity, indicating a similar mass doubling time across the galaxy's region. In our sample, we only have star-forming and green valley at this epoch. Quiescent galaxies emerge from $z \sim 3$ in our sample and we start to see more dispersion in the two ratios at this later epoch. At $1.5 \lesssim z \lesssim 2.5$ we see a large fraction of our star-forming galaxies have a compact star formation with $R_{e,\mathrm{SFR}}/R_e$ as low as ~ -0.5 dex and centrally-peaked sSFR with $\mathrm{sSFR_{in}/sSFR_{out}}$ of up to ~ 3 dex. In contrast to this, the majority of green valley and quiescent galaxies at this epoch have $R_{e,\mathrm{SFR}}/R_e > 1$ and $\mathrm{sSFR_{in}/sSFR_{out}} < 1$. At later epoch ($z \lesssim 1.5$), the majority of quiescent, green valley, and star-forming galaxies have extended SFR distributions and centrally-suppressed sSFR. The toy model has constant ratios of ~ 1 from the early epoch up to $z \sim 1.5$ after which its sSFR declines and SFR distribution becomes more extended. There is an indication that its $\mathrm{sSFR_{in}/sSFR_{out}}$ actually increases a little bit above 1 at $z \sim 1.5$.

The trends observed at $z \sim 0$ indicate that local spiral galaxies have overall extended SFR distributions and centrally-suppressed sSFR radial profiles. These trends agree with the scenarios inferred from our results in the current work and provide a nice extension to our results toward low redshift, complementing the general picture.

Overall, the above trend agrees with the inside-out growth and quenching scenarios. At early cosmic time, galaxies get steady gas accretion for star formation but they yet to form bulge and the star formation is likely distributed evenly across their regions. At $z \sim 2$, which coincides with the peak epoch of the cosmic SFRD and perhaps the cosmic gas accretion (Madau & Dickinson 2014), star-forming galaxies in our sample may experience gas compaction event that later build bulge in their centers. After that, quenching might has been started in their central regions, but star formation is still active in the disk that further build the disk. In addtion to in-situ star formation, minor mergers can also contribute to the buildup of stellar mass in the disk and grow the galaxy size.

5.2. *The buildup of the Central Stellar Mass Density Over Cosmic Time*

As we have seen in Section 4.4, our sample galaxies exhibit a tight relationship between the global M_* and the stellar mass surface density at the central 1 kpc $(\Sigma_{*,\mathrm{1kpc}})$. $\Sigma_{*,\mathrm{1kpc}}$ is a good indicator for quiescent galaxies because they form a rather distinct sequence at the tip of the overall M_*–$\Sigma_{*,\mathrm{1kpc}}$ relation and has a shallower slope. Here we discuss the evolution of $\Sigma_{*,\mathrm{1kpc}}$ with redshift to see how the central bulge is built over cosmic time in our sample galaxies. As $\Sigma_{*,\mathrm{1kpc}}$ develops over time, it is also interesting to analyze how sSFR at the central 1 kpc evolves following the development of $\Sigma_{*,\mathrm{1kpc}}$. The evolution of these two quantities are shown in Figure 14. As we can see from this figure, $\Sigma_{*,\mathrm{1kpc}}$ tend to increase with cosmic time, whereas $\mathrm{sSFR_{1kpc}}$ declines with cosmic time. The quiescent galaxies tend to have higher $\Sigma_{*,\mathrm{1kpc}}$ and lower $\mathrm{sSFR_{1kpc}}$ in all redshifts. $\mathrm{sSFR_{1kpc}}$ of quiescent and green-valley galaxies tend to be declined more rapidly than that of star-forming galaxies. Interestingly, the overall $\mathrm{sSFR_{1kpc}}$ of our star-forming galaxies does not decline much from $z = 6$ up to $z \sim 1.5$. There is an indication that $\mathrm{sSFR_{1kpc}}$ of some star-forming galaxies even increases at $1.5 \lesssim z \lesssim 2.5$.

The black profiles show expected evolution of Milky Way analogs based on our toy model derived in Section 5.1. Its $\Sigma_{*,\mathrm{1kpc}}$ increases by ~ 2 magnitude over $0.5 \lesssim z \lesssim 4.5$, while its $\mathrm{sSFR_{1kpc}}$ decreases significantly (~ 3.7 magnitude) over the same period. This implies that the central SFR within 1 kpc also decreases with time. At $1.5 \lesssim z \lesssim 2.5$, the $\mathrm{sSFR_{1kpc}}$ of this model seems to be constant. In addition to our toy model, we also compare our observational trend with the predictions from the VELA zoom-in cosmological hydrodynamical simulations (Ceverino et al. 2014; Zolotov et al. 2015) that was analyzed by Tacchella et al. (2016a).
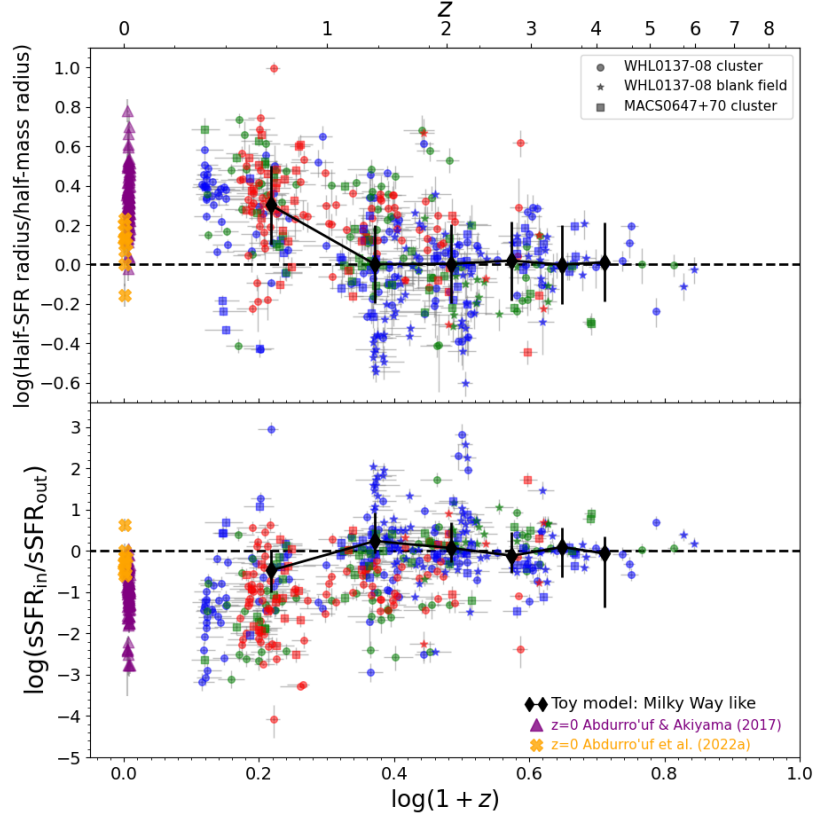
Figure 13. Evolution of the ratio between the half-SFR and half-mass radii (top panel) and the ratio between the sSFR inside and outise of the half-mass radius (bottom panel). The overall symbols and color-coding are the same as those in the right panel of Figure 5. The profiles shown with black diamond symbols represent an expectation from a toy empirical model for the evolution of the Milky Way analogs. For comparison, we also show the trends observed in local spiral galaxies from Abdurro'uf & Akiyama (2017) and Abdurro'uf et al. (2022a). At $z \gtrsim 3.5$, the two ratios are close to unity, indicating a similar mass doubling time across the galaxy's region. At $1.5 \lesssim z \lesssim 2.5$, many star-forming galaxies have a compact star formation ($R_{e,\mathrm{SFR}}/R_e$ as low as ~ -0.5 dex and $\mathrm{sSFR_{in}}/\mathrm{sSFR_{out}}$ up to ~ 3 dex). The majority of the green valley and quiescent galaxies at this epoch have $R_{e,\mathrm{SFR}}/R_e > 1$ and $\mathrm{sSFR_{in}}/\mathrm{sSFR_{out}} < 1$. At later epoch ($z \lesssim 1.5$), the majority of quiescent, green valley, and star-forming galaxies have extended SFR distributions and centrally-suppressed sSFR. Overall these trends point toward the inside-out growth and quenching scenario.

These predictions, which are shown in red profiles, are obtained by averaging the evolutionary trends of relatively massive galaxies in the simulations that have $\log(M_*/M_\odot) = 10.2$ at $z = 2$. This simulation was run over $1 < z < 7$. The $\Sigma_{*,1\mathrm{kpc}}$ and $\mathrm{sSFR_{1kpc}}$ predicted from the cosmological simulation at $z \sim 6$ are in good agreement with our observations. The evolution of the $\Sigma_{*,1\mathrm{kpc}}$ and $\mathrm{sSFR_{1kpc}}$ from the simulation seem to be consistent with the evolution of the progenitors of local massive quiescent galaxies, as implied from our observations. However, there is an excess of $\Sigma_{*,1\mathrm{kpc}}$ in $z \sim 0.5$ quiescent galaxies compared to the simulation. Those galaxies are likely members of the WHL0137−08 or MACS0647+70 clusters. In cluster, galaxies could accrete more mass through minor mergers which can result in denser stellar mass in their central regions.

The trends at $z \sim 0$ from Abdurro'uf & Akiyama (2017) and Abdurro'uf et al. (2022a) provide a good extension for our results in the current work. They overall agree with the picture of increasing $\Sigma_{*,1\mathrm{kpc}}$ and decreasing $\mathrm{sSFR_{1kpc}}$ with cosmic time. However, we also see a lower $\Sigma_{*,1\mathrm{kpc}}$ in the local spiral galaxies than in the quiescent galaxies at $z \sim 0.5$ that are possibly the cluster members. If we ignore these galaxies and assume that $\Sigma_{*,1\mathrm{kpc}}$ trend from the VELA simulation will evolve to have similar value as those of the observed $\Sigma_{*,1\mathrm{kpc}}$ of local galaxies (which is likely given its shallow slope at $z \sim 1$), we see a possible saturation of central mass density in galaxies.

Next, we compare between the effects of $\Sigma_{*,1\mathrm{kpc}}$ and the global M_* on $\mathrm{sSFR_{in}}/\mathrm{sSFR_{out}}$. We show the $\Sigma_{*,1\mathrm{kpc}}$–$\mathrm{sSFR_{in}}/\mathrm{sSFR_{out}}$ and M_*–$\mathrm{sSFR_{in}}/\mathrm{sSFR_{out}}$ rela-
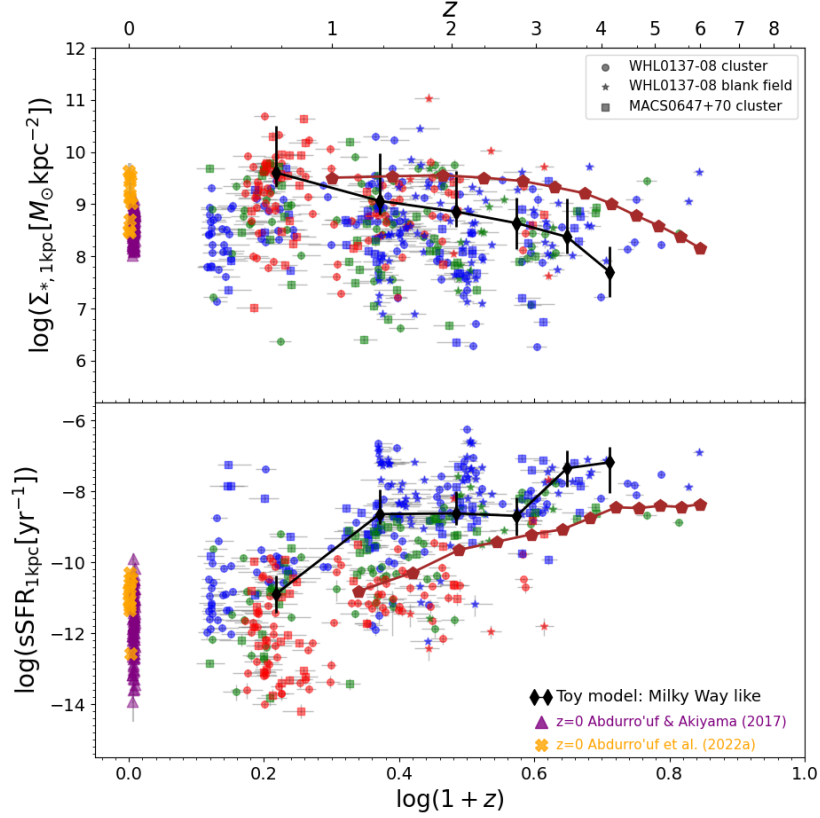
Figure 14. The builtup of the stellar mass density at the central 1 kpc ($\Sigma_{*,1\mathrm{kpc}}$) over cosmic time (top panel) and the evolution of sSFR at the central 1 kpc (sSFR$_{1\mathrm{kpc}}$; bottom panel). The profiles shown with black diamond symbols represent an expectation from a toy empirical model for the evolution of the Milky Way analogs, whereas the red pentagon symbols show a prediction from zoom-in cosmological hydrodynamical simulations by Tacchella et al. (2016a) for the evolution of massive galaxies ($\log(M_*(z=2)/M_\odot) > 10.2$).

tions in Figure 15. We can see from this figure that sSFR$_{\mathrm{in}}$/sSFR$_{\mathrm{out}}$ is correlated with both $\Sigma_{*,1\mathrm{kpc}}$ and the global M_* such that increasing $\Sigma_{*,1\mathrm{kpc}}$ and M_* correspond to a steeper sSFR decline in the central regions. However, the M_*–sSFR$_{\mathrm{in}}$/sSFR$_{\mathrm{out}}$ relation seems to be broader and less significant compared to M_*– sSFR$_{\mathrm{in}}$/sSFR$_{\mathrm{out}}$. The majority of those that have central sSFR suppression are the quiescent and green-valley galaxies, whereas a significant fraction of star-foroming galaxies have broadly flat or centrally-peaked sSFR radial profile (i.e., negative gradient). This further suggest that $\Sigma_{*,1\mathrm{kpc}}$ is a good predictor for quiescent galaxies.

6. SUMMARY AND CONCLUSIONS

We perform spatially resolved SED fitting on 444 galaxies at $0.3 < z < 6.0$ in two clusters (WHL0137−08 and MACS0647+70) and a blank field using imaging data from *JWST* and *HST* in up to 13 bands. We use PIXEDFIT throuhgout the analysis. This software can simultaneously perform image processing, pixel binning,

and spatially resolved SED fitting. By using the maps of spatially resolved stellar population properties (on kpc scales) obtained from this analysis, we investigate how galaxies grow their structures and quench their star formation activities across cosmic time. Overall, our key results are summarized in the following:

1. The normalization of the stellar mass surface density radial profiles ($\Sigma_{*,1\mathrm{kpc}}(r)$) increases with increasing cosmic time and global M_*. At each redshift, quiescent galaxies tend to have higher $\Sigma_{*,1\mathrm{kpc}}$ across the entire radius than green-valley and star-forming galaxies. The sSFR radial profiles (sSFR(r)) show more variations across redshift and global M_*. The sSFR(r) are broadly flat at $2.5 \lesssim z \lesssim 6.0$ in all galaxies. At $0.8 \lesssim z \lesssim 2.5$, less massive ($\log(M_*/M_\odot) < 11.0$) star-forming galaxies have flat or centrally-peaked sSFR(r), whereas the majority of quiescent galaxies have centrally-suppressed sSFR(r). At lower redshift ($z < 0.8$), almost all galaxies (regardless of M_* and
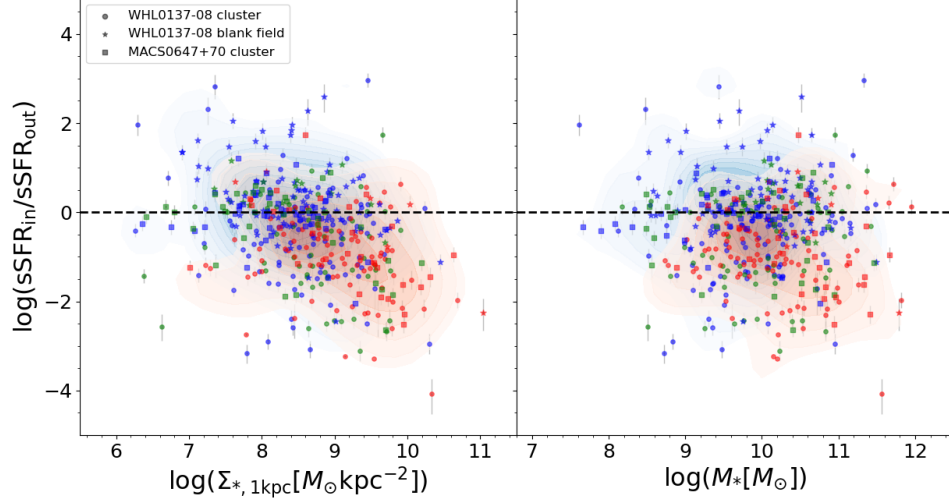
Figure 15. The $\mathrm{sSFR_{in}}/\mathrm{sSFR_{out}}$ ratio as a function of the central mass density (left panel) and global M_*(right panel). The overall symbols in this figure is the same as those in Figure 10. Galaxies that are massive and have high $\Sigma_{*,\mathrm{1kpc}}$ tend to have centrally-suppressed sSFR profiles. This trend is predominantly observed in quiescent galaxies.

star formation stage) have centrally-suppressed $\mathrm{sSFR}(r)$. The radial profiles of stellar ages show that those galaxies with centrally-peaked $\mathrm{sSFR}(r)$ have very young stellar populations in their central regions, indicating an on-going nuclear starburst. We also see an increasing normalization of age radial profiles and flattening of their slopes with increasing cosmic time.

2. The majority of quiescent galaxies have larger half-SFR radius than half-mass radius, indicating that they have extended spatial distribution of SFR and compact distribution of stellar mass. In contrast, some star-forming galaxies, especially at high redshifts, have half-SFR radius being roughly similar or smaller to half-mass radius, whereas those at low redshifts have half-SFR radius being larger than half-mass radius. The half-mass radius of the star-forming galaxies is on average larger than the quiescent galaxies in all global M_*.

3. We observe a tight correlation between the global M_* and stellar mass density at the central 1 kpc ($\Sigma_{*,\mathrm{1kpc}}$) with 0.38 dex, indicating that galaxies grow their central mass density hand-in-hand with their global M_*. The quiescent galaxies reside in a sequence at the tip of the overall relation and have a shallower slope. This trend indicates that $\Sigma_{*,\mathrm{1kpc}}$ is a good predictor of quenching, where passive galaxies tend to have higher $\Sigma_{*,\mathrm{1kpc}}$ and global M_*. The shallower slope of M_*–$\Sigma_{*,\mathrm{1kpc}}$ in quiescent galaxies suggest that their central mass

density has reached a saturation point (i.e., a mature bulge has been formed).

4. We investigate the evolution of the $R_{e,\mathrm{SFR}}/R_e$ and $\mathrm{sSFR_{in}}/\mathrm{sSFR_{out}}$ ratios with redshift to try to understand how galaxies grow their structures and quench their star formations over cosmic time. We find that the ratios are close to unity from the early epoch up to $z \sim 3.5$ and the ratios start to deviate from unity since then. At $1.5 \lesssim z \lesssim 2.5$, a fraction of our star-forming sample has a low $R_{e,\mathrm{SFR}}/R_e$ and high $\mathrm{sSFR_{in}}/\mathrm{sSFR_{out}}$, indicating that they may be experiencing a nuclear starburst. At the later epoch, most of our sample galaxies, especially quiescent and green-valley have a high $R_{e,\mathrm{SFR}}/R_e$ and low $\mathrm{sSFR_{in}}/\mathrm{sSFR_{out}}$, suggesting that massive bulges might have been formed in these galaxies and the star formation has been quenched in their central regions.

5. We also investigate the evolution of $\Sigma_{*,\mathrm{1kpc}}$ and sSFR at the central 1 kpc ($\mathrm{sSFR_{1kpc}}$). In general, we see an increasing $\Sigma_{*,\mathrm{1kpc}}$ and decreasing $\mathrm{sSFR_{1kpc}}$ with cosmic time, indicating the buildup of the central bulge component and the quenching process in the central region of the galaxies. We also find that quiescent galaxies tend to have higher $\Sigma_{*,\mathrm{1kpc}}$ and lower $\mathrm{sSFR_{1kpc}}$ than star-forming galaxies in all redshifts.

6. Finally, we find a relationship between $\Sigma_{*,\mathrm{1kpc}}$ and $\mathrm{sSFR_{in}}/\mathrm{sSFR_{out}}$ with a negative slope, indicating that galaxies that have more massive $\Sigma_{*,\mathrm{1kpc}}$ tend to have steeper central suppression in their sSFR

radial profiles. The quiescent galaxies tend to have higher $\Sigma_{*,1\mathrm{kpc}}$ and $\mathrm{sSFR_{in}}/\mathrm{sSFR_{out}} < 1$, suggesting that the formation of bulge might happen simultaneously with the quenching of star formation in the central regions.

Our study in this paper demonstrates the great potentials of spatially resolved SED analysis using *JWST* imaging data. It is interesting to extend this study with larger sample galaxies taken from various surveys to better understand the buildup of stellar mass in galaxies and the growth of their structures over cosmic time. More comprehensive comparisons with zoom-in cosmological simulations would help to better understand the underlying physics. We will pursue this in our future works.

APPENDIX

A. ROBUSTNESS OF THE SED FITTING METHOD: FITTING TESTS WITH MOCK SEDS

To test the robustness of our SED fitting method on this new set of photometric data, we perform SED-fitting tests using semiempirical mock SEDs, following a similar procedure as performed in Abdurro'uf et al. (2022a, Appendix A therein). We draw the parameter values for our mock SEDs from the measured parameters of real galaxies. In this case, we use the measured parameters obtained from our fitting to the SEDs within the central effective radius that were used for determining our photometric redshifts (see Section 3.5). Here, we use 290 galaxies selected randomly from 354 galaxies in the WHL0137−08 (before further exclusion). We prefer to use the parameters of real galaxies for generating mock SEDs, instead of drawing them randomly because we can not be sure that the combinations of those random parameters are physically realistic. Using the set of parameters of 290 galaxies, we generate mock SEDs using the same modeling setup as in our main analysis. We generate two sets of mock SEDs. The first one with 12 filters of *JWST* and *HST*, the same set of filters as available for the WHL0137−08 cluster. The second set with 8 *JWST* filters, excluding *HST* filters. We then inject Gaussian noises assuming S/N of 20 in all filters. After that, we fit the mock SEDs using the same method as we used in the main analysis of this paper. For simplicity, here we fix redshift.

We present the results in Figure 16, which shows the comparisons between the best-fit parameters derived from SED fitting and the true values form the mock SEDs. Histograms in the insets show ratios between the best-fit parameters and the true values. Results of the SED fitting with two sets of photometry are shown with different symbols and the histograms are shown with different colors. The data points are color-coded based on their redshifts.
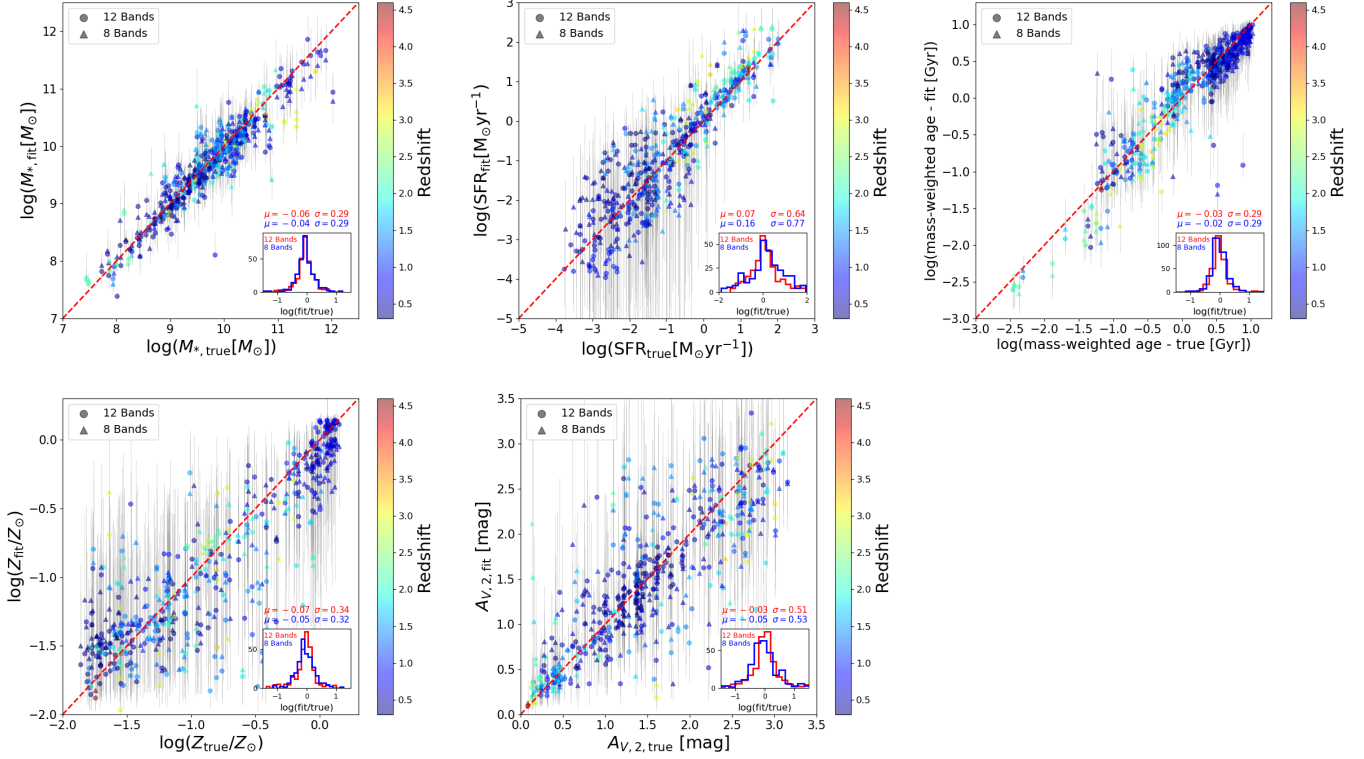
Figure 16. Comparisons between the best-fit parameters derived from SED-fitting tests using mock SEDs and the ground truth. In this test, two sets of photometry are used, one with combined 12 filters of *HST* and *JWST* and the other with 8 filters of *JWST* only. The results of those two SED fitting tests are shown with different symbols (circle and squares). Histograms in the insets show ratios between the best-fit parameters and the true values from the mock SEDs. The color-coding of the data points represents redshift.

Overall, our SED fitting can recover the true parameters reasonably well. Stellar mass and mass-weighted age are recovered very well in both 8-band and 12-band SED fitting with small offset ($\lesssim 0.06$ dex) and small standard deviation ($\lesssim 0.3$ dex). It is interesting to see that mass-weighed age is well recovered here. This may be due to the fact that our photometry covers the Balmer break and we have good photometry in rest-frame NIR from *JWST*, which also provides good constraint for M_* (see Appendix B). The stellar metallicity (Z) and dust attenuation in the diffuse ISM ($A_{V,2}$) are also recovered well with an offset of $\lesssim 0.07$ dex and a standard deviation of $\lesssim 0.5$ dex although they look to be more scattered due to its small dynamical range. The SFR is more difficult to be recovered for passive galaxies ($\log(\text{SFR}) \lesssim -1$) than for star-forming ones. For whole sample, the SED fitting with 12 bands gives better SFR estimates (a small offset of 0.07 dex and scatter of 0.64 dex) than with only *JWST* bands (offset of 0.16 dex and scatter of 0.77 dex).

B. THE AGE–DUST–METALLICITY DEGENERACIES

The addition of the *JWST* NIRCam data extends the wavelength coverage up to roughly the rest-frame NIR for our sample galaxies. This sufficiently wide wavelength coverage has a potential to break the well-known age–dust–metallicity degeneracy in SED fitting, which is very important for the analysis in this paper. In particular, it is crucial to be able to determine if the reddening observed in the central region of some galaxies in our sample is due to aging (i.e., quiescence) or the dust attenuation. To check if our data set provides a sufficient constraint for resolving this degeneracy, we examine model color-color diagrams among the NIRCam filters. We base our analysis on the observed-frame, instead of the rest-frame, and explore different sets of filters for different redshifts. To generate model SEDs, we use overall similar setting as that used in the main analysis of this paper and assume a double power-law SFH with $\alpha = 3.0$, $\beta = 0.5$, and $\tau = 1.5$ Gyr, and $M_* = 10^{10.5} M_\odot$. We then generate model SEDs in grids of age, $A_{V,2}$, and metallicity. For simplicity, we assume $A_{V,1} = 1.5 \times A_{V,2}$.
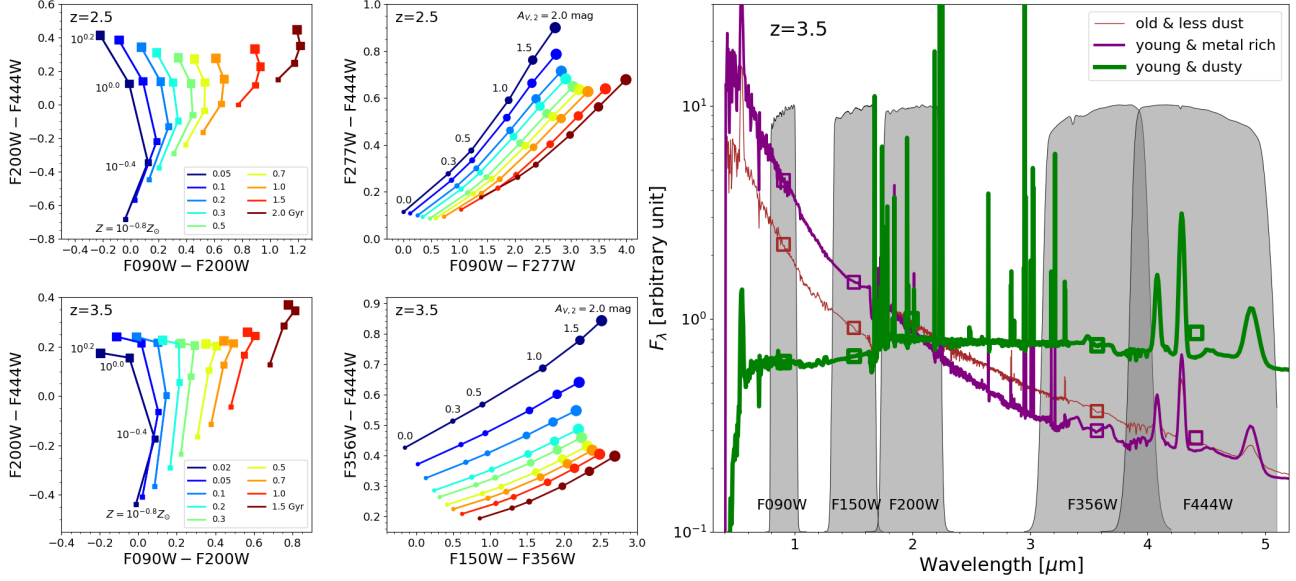
Figure 17. The patterns of model stellar populations on the observed-frame color-color diagrams involving *JWST* NIRCam filters. We plot the patterns of models at $z = 2.5$ and $z = 3.5$ on the color-color diagrams to check how good the NIRCam photometry in resolving the degeneracies among age, dust attenuation, and metallicity in high redshifts. Different colors represent different age, whereas an increasing marker size represents an increasing Z (for square symbol) and increasing $A_{V,2}$ (for circle symbol). The rightmost panel shows examples of the model SEDs of old less-dusty (brown color), young metal-rich (purple), and young dusty (green) galaxies at $z = 3.5$. The reddening effects by aging and dust are almost orthogonal with each other (i.e., distinguishable) on the F090W−F200W vs. F200W−F444W diagram. The reddening effects by aging and dust attenuation are distinguishable on the F090W−F277W vs. F277W−F444W for $z = 2.5$ and the F150W−F356W vs. F356W−F444W for $z = 3.5$.

Figure 17 shows the color-color diagrams of models at $z = 2.5$ and 3.5. Different colors represent different ages, whereas increasing marker size represents increasing metallicity (for square symbol in the first column) and $A_{V,2}$ (for circle symbol in the second column). For the two plots in the first column, we fix $A_{V,2} = 0.0$, whereas for the two plots in the second column, we fix $Z = Z_\odot$. F090W−F200W vs. F200W−F444W diagram at the two redshifts seems to be able to distinguish the reddening effect by age and metallicity in such a way that the both effects are almost orthogonal with each other. An increasing Z at a fixed age corresponds to reddening in F200W−F444W and roughly constant F090W−F200W (i.e., vertical shift on the diagram). On the other hand, an increasing age tends to make reddening in the two colors (i.e., a diagonal shift on the diagram) for galaxies with low Z, while it corresponds to a roughly horizontal shift for galaxies with high Z. In the second column, we show a relative effect of the dust attenuation and aging on F090W−F277W vs. F277W−F444W (for $z = 2.5$) and F150W−F356W vs. F356W−F444W (for $z = 3.5$) diagrams. The two effects are distinguishable in these two diagrams with dust attenuation seem to make a diagonal shift, whereas an aging effect is roughly orthogonal to it. For an illustration, in the rightmost panel we show examples of the model SEDs of an old less-dusty (brown color; age1.5 Gyr, $\log(Z/Z_\odot) = -0.5$, $A_{V,2} = 0.1$ mag), young metal-rich (purple; age0.1 Gyr, $\log(Z/Z_\odot) = 0.2$, $A_{V,2} = 0.1$ mag), and young dusty (green; age0.1 Gyr, $\log(Z/Z_\odot) = -0.5$, $A_{V,2} = 2.0$ mag) galaxies $z = 3.5$. We normalize the SEDs by dividing them with the F200W flux. We also show the transmission curves of the filters that are used in the color-color diagrams for $z = 3.5$ in the left two columns. As we can see from this figure, the three model SEDs are distinguishable with NIRCam photometry. The reddening due to the dust attenuation is easily recognisable in the rest-frame UV to NIR, while that due to the metallicity is not easily recognisable in the rest-frame UV colors but it is detectable in the rest-frame around the Balmer break (~ 4000 Å) and NIR.

C. CONSTRUCTION OF EMPIRICAL POINT SPREAD FUNCTIONS AND CONVOLUTION KERNELS

We generate the empirical PSFs of the *HST* ACS and *JWST* NIRcam filters in the WHL0137−08 and MACS0647+70 clusters by stacking images of the bright isolated stars in those fields. For this, we use some functions in PHOTUTILS

package (Bradley et al. 2022a). We show the encircled energy of the empirical PSFs in the left column of Figure 18. After generating the PSFs, we then construct the convolution kernels that can be used for PSF matching. As described in Section 3.2, we perform PSF matching to homogenize the PSF sizes of our imaging data to match the F444W PSF, which is the largest among the filters used in our work. We also use PHOTUTILS for generating the kernels. To check the reliability of our kernels and PSF matching, we convolve the PSF images of the filters other than F444W with the kernels and compare the encircled energy of the convolved-PSFs to that of F444W filter. We show this comparison in the right column of Figure 18. As we can see from this figure, there is an overall good agreement among the encircle energy after the PSF matching. We note that there is a small deviation (< 0.1 dex) around a radius of $0.''1$.
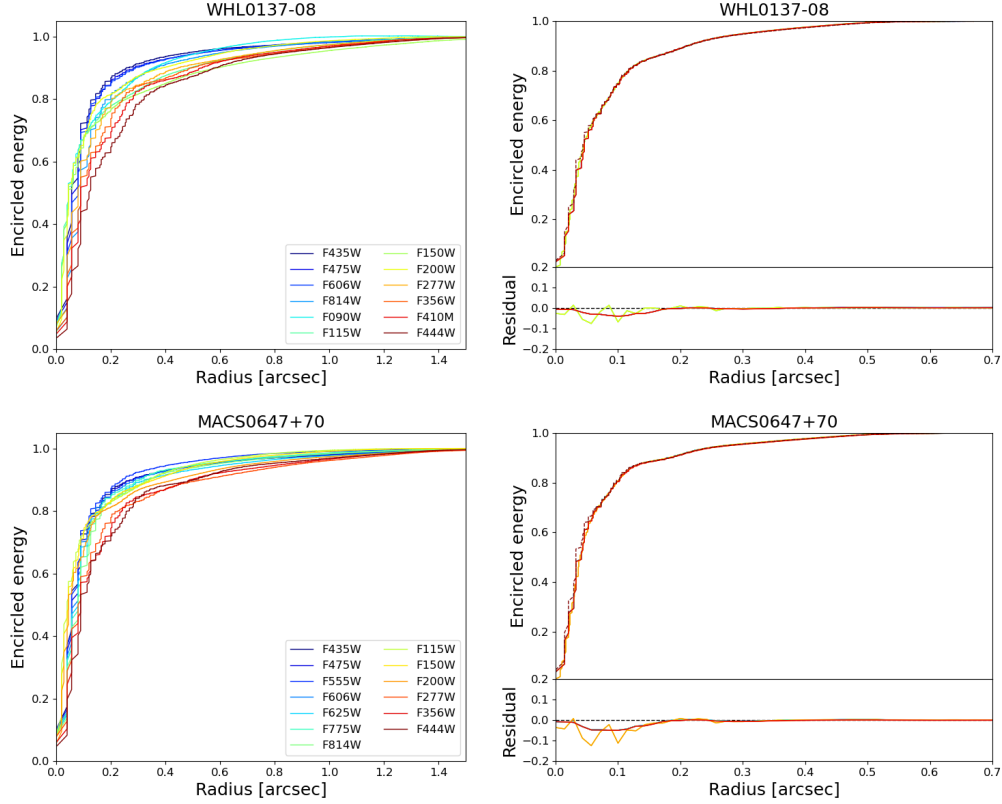
Figure 18. *Left column*: the encircled energy of the empirical PSFs of the *HST* ACS and *JWST* NIRCam filters in WHL0137−08 and MACS0647+70 clusters. The PSFs are generated by stacking the images of bright isolated stars in the fields. *Right column*: the encircled energy of the PSFs after PSF matching process, which homogenize the PSF sizes to match the F444W PSF.

REFERENCES

Abdurro'uf, & Akiyama, M. 2017, MNRAS, 469, 2806, doi: 10.1093/mnras/stx936

—. 2018, MNRAS, 479, 5083, doi: 10.1093/mnras/sty1771

Abdurro'uf, Lin, Y.-T., Hirashita, H., et al. 2022a, ApJ, 926, 81, doi: 10.3847/1538-4357/ac439a

—. 2022b, ApJ, 935, 98, doi: 10.3847/1538-4357/ac7da4

Abdurro'uf, Lin, Y.-T., Wu, P.-F., & Akiyama, M. 2021, ApJS, 254, 15, doi: 10.3847/1538-4365/abebe2

—. 2022c, piXedfit: Analyze spatially resolved SEDs of galaxies, Astrophysics Source Code Library, record ascl:2207.033. http://ascl.net/2207.033

Astropy Collaboration, Robitaille, T. P., Tollerud, E. J., et al. 2013, A&A, 558, A33, doi: 10.1051/0004-6361/201322068

Astropy Collaboration, Price-Whelan, A. M., Sipőcz, B. M., et al. 2018, AJ, 156, 123, doi: 10.3847/1538-3881/aabc4f

Astropy Collaboration, Price-Whelan, A. M., Lim, P. L., et al. 2022, ApJ, 935, 167, doi: 10.3847/1538-4357/ac7c74

28

Aumer, M., & White, S. D. M. 2013, MNRAS, 428, 1055,
doi: 10.1093/mnras/sts083

Barbary, K. 2016, Journal of Open Source Software, 1, 58,
doi: 10.21105/joss.00058

Barro, G., Faber, S. M., Koo, D. C., et al. 2017, ApJ, 840,
47, doi: 10.3847/1538-4357/aa6b05

Bertin, E., & Arnouts, S. 1996, A&AS, 117, 393,
doi: 10.1051/aas:1996164

Birnboim, Y., & Dekel, A. 2003, MNRAS, 345, 349,
doi: 10.1046/j.1365-8711.2003.06955.x

Bouché, N., Dekel, A., Genzel, R., et al. 2010, ApJ, 718,
1001, doi: 10.1088/0004-637X/718/2/1001

Boyer, M. L., Anderson, J., Gennaro, M., et al. 2022, arXiv
e-prints, arXiv:2209.03348.
https://arxiv.org/abs/2209.03348

Bradley, L., Sipőcz, B., Robitaille, T., et al. 2022a,
astropy/photutils: 1.5.0, 1.5.0, Zenodo, Zenodo,
doi: 10.5281/zenodo.6825092

Bradley, L. D., Coe, D., Brammer, G., et al. 2022b, arXiv
e-prints, arXiv:2210.01777.
https://arxiv.org/abs/2210.01777

Brammer, G., Strait, V., Matharu, J., & Momcheva, I.
2022, grizli, 1.5.0, Zenodo, doi: 10.5281/zenodo.6672538

Brammer, G. B., van Dokkum, P. G., & Coppi, P. 2008,
ApJ, 686, 1503, doi: 10.1086/591786

Brinchmann, J., Charlot, S., White, S. D. M., et al. 2004,
MNRAS, 351, 1151,
doi: 10.1111/j.1365-2966.2004.07881.x

Broadhurst, T., Benítez, N., Coe, D., et al. 2005, ApJ, 621,
53, doi: 10.1086/426494

Bundy, K., Bershady, M. A., Law, D. R., et al. 2015, ApJ,
798, 7, doi: 10.1088/0004-637X/798/1/7

Cano-Díaz, M., Sánchez, S. F., Zibetti, S., et al. 2016,
ApJL, 821, L26, doi: 10.3847/2041-8205/821/2/L26

Casey, C. M., Zavala, J. A., Spilker, J., et al. 2018, ApJ,
862, 77, doi: 10.3847/1538-4357/aac82d

Ceverino, D., Klypin, A., Klimek, E. S., et al. 2014,
MNRAS, 442, 1545, doi: 10.1093/mnras/stu956

Chabrier, G. 2003, PASP, 115, 763, doi: 10.1086/376392

Chan, B. M. Y., Broadhurst, T., Lim, J., et al. 2017, ApJ,
835, 44, doi: 10.3847/1538-4357/835/1/44

Charlot, S., & Fall, S. M. 2000, ApJ, 539, 718,
doi: 10.1086/309250

Chen, C.-C., Gao, Z.-K., Hsu, Q.-N., et al. 2022, ApJL,
939, L7, doi: 10.3847/2041-8213/ac98c6

Coe, D., Fuselier, E., Benítez, N., et al. 2008, ApJ, 681,
814, doi: 10.1086/588250

Coe, D., Umetsu, K., Zitrin, A., et al. 2012, ApJ, 757, 22,
doi: 10.1088/0004-637X/757/1/22

Coe, D., Zitrin, A., Carrasco, M., et al. 2013, ApJ, 762, 32,
doi: 10.1088/0004-637X/762/1/32

Coe, D., Salmon, B., Bradač, M., et al. 2019, ApJ, 884, 85,
doi: 10.3847/1538-4357/ab412b

Cole, S., Lacey, C. G., Baugh, C. M., & Frenk, C. S. 2000,
MNRAS, 319, 168, doi: 10.1046/j.1365-8711.2000.03879.x

Conroy, C., & Gunn, J. E. 2010, ApJ, 712, 833,
doi: 10.1088/0004-637X/712/2/833

Conroy, C., Gunn, J. E., & White, M. 2009, ApJ, 699, 486,
doi: 10.1088/0004-637X/699/1/486

Daddi, E., Dickinson, M., Morrison, G., et al. 2007, ApJ,
670, 156, doi: 10.1086/521818

Daddi, E., Bournaud, F., Walter, F., et al. 2010, ApJ, 713,
686, doi: 10.1088/0004-637X/713/1/686

Dayal, P., & Ferrara, A. 2018, PhR, 780, 1,
doi: 10.1016/j.physrep.2018.10.002

Dekel, A., & Birnboim, Y. 2006, MNRAS, 368, 2,
doi: 10.1111/j.1365-2966.2006.10145.x

Dekel, A., & Burkert, A. 2014, MNRAS, 438, 1870,
doi: 10.1093/mnras/stt2331

Diego, J. M., Protopapas, P., Sandvik, H. B., & Tegmark,
M. 2005, MNRAS, 360, 477,
doi: 10.1111/j.1365-2966.2005.09021.x

Diego, J. M., Tegmark, M., Protopapas, P., & Sandvik,
H. B. 2007, MNRAS, 375, 958,
doi: 10.1111/j.1365-2966.2007.11380.x

Ebeling, H., Barrett, E., Donovan, D., et al. 2007, ApJL,
661, L33, doi: 10.1086/518603

Elbaz, D., Daddi, E., Le Borgne, D., et al. 2007, A&A, 468,
33, doi: 10.1051/0004-6361:20077525

Falcón-Barroso, J., Sánchez-Blázquez, P., Vazdekis, A.,
et al. 2011, A&A, 532, A95,
doi: 10.1051/0004-6361/201116842

Fang, J. J., Faber, S. M., Koo, D. C., & Dekel, A. 2013,
ApJ, 776, 63, doi: 10.1088/0004-637X/776/1/63

Ferland, G. J., Korista, K. T., Verner, D. A., et al. 1998,
PASP, 110, 761, doi: 10.1086/316190

Ferland, G. J., Porter, R. L., van Hoof, P. A. M., et al.
2013, RMxAA, 49, 137. https://arxiv.org/abs/1302.4485

Ferreira, L., Adams, N., Conselice, C. J., et al. 2022, ApJL,
938, L2, doi: 10.3847/2041-8213/ac947c

Finkelstein, S. L., Bagley, M. B., Ferguson, H. C., et al.
2022, arXiv e-prints, arXiv:2211.05792.
https://arxiv.org/abs/2211.05792

Förster Schreiber, N. M., Renzini, A., Mancini, C., et al.
2018, ApJS, 238, 21, doi: 10.3847/1538-4365/aadd49

Fudamoto, Y., Oesch, P. A., Schouws, S., et al. 2021,
Nature, 597, 489, doi: 10.1038/s41586-021-03846-z

Gaia Collaboration, Brown, A. G. A., Vallenari, A., et al.
2021, A&A, 649, A1, doi: 10.1051/0004-6361/202039657

Genzel, R., Tacconi, L. J., Gracia-Carpio, J., et al. 2010, MNRAS, 407, 2091, doi: 10.1111/j.1365-2966.2010.16969.x

Giménez-Arteaga, C., Oesch, P. A., Brammer, G. B., et al. 2022, arXiv e-prints, arXiv:2212.08670. https://arxiv.org/abs/2212.08670

Girardi, L., Bressan, A., Bertelli, G., & Chiosi, C. 2000, A&AS, 141, 371, doi: 10.1051/aas:2000126

Hoffmann, S. L., Mack, J., Avila, R., et al. 2021, in American Astronomical Society Meeting Abstracts, Vol. 53, American Astronomical Society Meeting Abstracts, 216.02

Hsiao, T. Y.-Y., Coe, D., Abdurro'uf, et al. 2022, arXiv e-prints, arXiv:2210.14123. https://arxiv.org/abs/2210.14123

Hsieh, B. C., Lin, L., Lin, J. H., et al. 2017, ApJL, 851, L24, doi: 10.3847/2041-8213/aa9d80

Inoue, A. K., Shimizu, I., Iwata, I., & Tanaka, M. 2014, MNRAS, 442, 1805, doi: 10.1093/mnras/stu936

Iyer, K., Gawiser, E., Davé, R., et al. 2018, ApJ, 866, 120, doi: 10.3847/1538-4357/aae0fa

Jullo, E., & Kneib, J. P. 2009, MNRAS, 395, 1319, doi: 10.1111/j.1365-2966.2009.14654.x

Jullo, E., Kneib, J. P., Limousin, M., et al. 2007, New Journal of Physics, 9, 447, doi: 10.1088/1367-2630/9/12/447

Jung, I., Finkelstein, S. L., Song, M., et al. 2017, ApJ, 834, 81, doi: 10.3847/1538-4357/834/1/81

Kartaltepe, J. S., Rose, C., Vanderhoof, B. N., et al. 2022, arXiv e-prints, arXiv:2210.14713. https://arxiv.org/abs/2210.14713

Kereš, D., Katz, N., Weinberg, D. H., & Davé, R. 2005, MNRAS, 363, 2, doi: 10.1111/j.1365-2966.2005.09451.x

Kneib, J. P., Mellier, Y., Fort, B., & Mathez, G. 1993, A&A, 273, 367

Koekemoer, A. M., Fruchter, A. S., Hook, R. N., & Hack, W. 2003, in HST Calibration Workshop : Hubble after the Installation of the ACS and the NICMOS Cooling System, 337

Leja, J., Speagle, J. S., Ting, Y.-S., et al. 2022, ApJ, 936, 165, doi: 10.3847/1538-4357/ac887d

Lin, L., Pan, H.-A., Ellison, S. L., et al. 2019, ApJL, 884, L33, doi: 10.3847/2041-8213/ab4815

Madau, P., & Dickinson, M. 2014, ARA&A, 52, 415, doi: 10.1146/annurev-astro-081811-125615

Marigo, P., & Girardi, L. 2007, A&A, 469, 239, doi: 10.1051/0004-6361:20066772

Marigo, P., Girardi, L., Bressan, A., et al. 2008, A&A, 482, 883, doi: 10.1051/0004-6361:20078467

McGreer, I. D., Mesinger, A., & D'Odorico, V. 2015, MNRAS, 447, 499, doi: 10.1093/mnras/stu2449

Meena, A. K., Zitrin, A., Jiménez-Teja, Y., et al. 2022, arXiv e-prints, arXiv:2211.13334. https://arxiv.org/abs/2211.13334

Morishita, T., Ichikawa, T., & Kajisawa, M. 2014, ApJ, 785, 18, doi: 10.1088/0004-637X/785/1/18

Morishita, T., Ichikawa, T., Noguchi, M., et al. 2015, ApJ, 805, 34, doi: 10.1088/0004-637X/805/1/34

Morselli, L., Rodighiero, G., Enia, A., et al. 2020, MNRAS, 496, 4606, doi: 10.1093/mnras/staa1811

Nardiello, D., Bedin, L. R., Burgasser, A., et al. 2022, arXiv e-prints, arXiv:2209.06547. https://arxiv.org/abs/2209.06547

Nelson, E. J., van Dokkum, P. G., Brammer, G., et al. 2012, ApJL, 747, L28, doi: 10.1088/2041-8205/747/2/L28

Nelson, E. J., van Dokkum, P. G., Förster Schreiber, N. M., et al. 2016, ApJ, 828, 27, doi: 10.3847/0004-637X/828/1/27

Noeske, K. G., Weiner, B. J., Faber, S. M., et al. 2007, ApJL, 660, L43, doi: 10.1086/517926

Oguri, M. 2010, PASJ, 62, 1017, doi: 10.1093/pasj/62.4.1017

Pascale, M., Frye, B. L., Diego, J., et al. 2022, ApJL, 938, L6, doi: 10.3847/2041-8213/ac9316

Peng, C. Y., Ho, L. C., Impey, C. D., & Rix, H.-W. 2002, AJ, 124, 266, doi: 10.1086/340952

Postman, M., Coe, D., Benítez, N., et al. 2012, ApJS, 199, 25, doi: 10.1088/0067-0049/199/2/25

Rigby, J., Perrin, M., McElwain, M., et al. 2022, arXiv e-prints, arXiv:2207.05632. https://arxiv.org/abs/2207.05632

Roberts-Borsani, G., Treu, T., Chen, W., et al. 2022, arXiv e-prints, arXiv:2210.15639. https://arxiv.org/abs/2210.15639

Salmon, B., Papovich, C., Finkelstein, S. L., et al. 2015, ApJ, 799, 183, doi: 10.1088/0004-637X/799/2/183

Sánchez, S. F. 2020, ARA&A, 58, 99, doi: 10.1146/annurev-astro-012120-013326

Sánchez, S. F., Rosales-Ortega, F. F., Jungwiert, B., et al. 2013, A&A, 554, A58, doi: 10.1051/0004-6361/201220669

Sánchez-Blázquez, P., Peletier, R. F., Jiménez-Vicente, J., et al. 2006, MNRAS, 371, 703, doi: 10.1111/j.1365-2966.2006.10699.x

Santini, P., Fontana, A., Castellano, M., et al. 2017, ApJ, 847, 76, doi: 10.3847/1538-4357/aa8874

Shen, S., Mo, H. J., White, S. D. M., et al. 2003, MNRAS, 343, 978, doi: 10.1046/j.1365-8711.2003.06740.x

Skelton, R. E., Whitaker, K. E., Momcheva, I. G., et al. 2014, ApJS, 214, 24, doi: 10.1088/0067-0049/214/2/24

30

Speagle, J. S., Steinhardt, C. L., Capak, P. L., & Silverman, J. D. 2014, ApJS, 214, 15, doi: 10.1088/0067-0049/214/2/15

Suess, K. A., Kriek, M., Price, S. H., & Barro, G. 2019, ApJ, 877, 103, doi: 10.3847/1538-4357/ab1bda

Tacchella, S., Dekel, A., Carollo, C. M., et al. 2016a, MNRAS, 458, 242, doi: 10.1093/mnras/stw303

—. 2016b, MNRAS, 457, 2790, doi: 10.1093/mnras/stw131

Tacchella, S., Forbes, J. C., & Caplar, N. 2020, MNRAS, 497, 698, doi: 10.1093/mnras/staa1838

Tacchella, S., Carollo, C. M., Renzini, A., et al. 2015, Science, 348, 314, doi: 10.1126/science.1261094

Tacchella, S., Carollo, C. M., Förster Schreiber, N. M., et al. 2018, ApJ, 859, 56, doi: 10.3847/1538-4357/aabf8b

Tomczak, A. R., Quadri, R. F., Tran, K.-V. H., et al. 2016, ApJ, 817, 118, doi: 10.3847/0004-637X/817/2/118

Treu, T., Schmidt, K. B., Trenti, M., Bradley, L. D., & Stiavelli, M. 2013, ApJL, 775, L29, doi: 10.1088/2041-8205/775/1/L29

van den Bosch, F. C. 2002, MNRAS, 332, 456, doi: 10.1046/j.1365-8711.2002.05328.x

van der Wel, A., Franx, M., van Dokkum, P. G., et al. 2014, ApJ, 788, 28, doi: 10.1088/0004-637X/788/1/28

van Dokkum, P. G., Whitaker, K. E., Brammer, G., et al. 2010, ApJ, 709, 1018, doi: 10.1088/0004-637X/709/2/1018

van Dokkum, P. G., Leja, J., Nelson, E. J., et al. 2013, ApJL, 771, L35, doi: 10.1088/2041-8205/771/2/L35

van Dokkum, P. G., Nelson, E. J., Franx, M., et al. 2015, ApJ, 813, 23, doi: 10.1088/0004-637X/813/1/23

Vanzella, E., Claeyssens, A., Welch, B., et al. 2022, arXiv e-prints, arXiv:2211.09839. https://arxiv.org/abs/2211.09839

Welch, B., Coe, D., Diego, J. M., et al. 2022a, Nature, 603, 815, doi: 10.1038/s41586-022-04449-y

Welch, B., Coe, D., Zackrisson, E., et al. 2022b, arXiv e-prints, arXiv:2208.09007. https://arxiv.org/abs/2208.09007

Wen, Z. L., & Han, J. L. 2015, ApJ, 807, 178, doi: 10.1088/0004-637X/807/2/178

Wen, Z. L., Han, J. L., & Liu, F. S. 2012, ApJS, 199, 34, doi: 10.1088/0067-0049/199/2/34

Whitaker, K. E., van Dokkum, P. G., Brammer, G., & Franx, M. 2012, ApJL, 754, L29, doi: 10.1088/2041-8205/754/2/L29

Whitaker, K. E., Franx, M., Leja, J., et al. 2014, ApJ, 795, 104, doi: 10.1088/0004-637X/795/2/104

Whitaker, K. E., Bezanson, R., van Dokkum, P. G., et al. 2017, ApJ, 838, 19, doi: 10.3847/1538-4357/aa6258

Williams, H., Kelly, P. L., Chen, W., et al. 2022, arXiv e-prints, arXiv:2210.15699. https://arxiv.org/abs/2210.15699

Wuyts, S., Förster Schreiber, N. M., Nelson, E. J., et al. 2013, ApJ, 779, 135, doi: 10.1088/0004-637X/779/2/135

Yang, L., Roberts-Borsani, G., Treu, T., et al. 2021, MNRAS, 501, 1028, doi: 10.1093/mnras/staa3713

Zitrin, A., Broadhurst, T., Barkana, R., Rephaeli, Y., & Benítez, N. 2011, MNRAS, 410, 1939, doi: 10.1111/j.1365-2966.2010.17574.x

Zitrin, A., Broadhurst, T., Umetsu, K., et al. 2009, MNRAS, 396, 1985, doi: 10.1111/j.1365-2966.2009.14899.x

Zitrin, A., Fabris, A., Merten, J., et al. 2015, ApJ, 801, 44, doi: 10.1088/0004-637X/801/1/44

Zolotov, A., Dekel, A., Mandelker, N., et al. 2015, MNRAS, 450, 2327, doi: 10.1093/mnras/stv740